

AD-A158 823

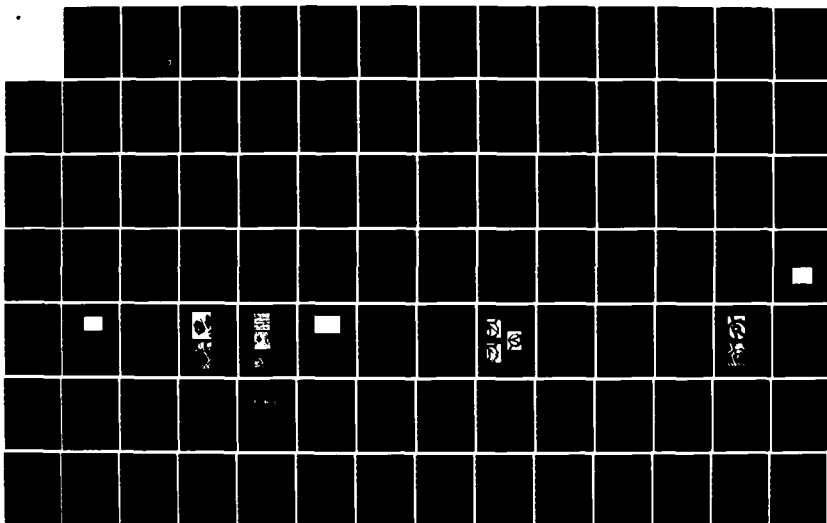
PHOTOACOUSTIC IMAGING(U) STANFORD UNIV CA EDWARD L
GINZTON LAB OF PHYSICS C C WILLIAMS ET AL. OCT 84
GL-3777 AFOSR-TR-85-0124 AFOSR-82-0248

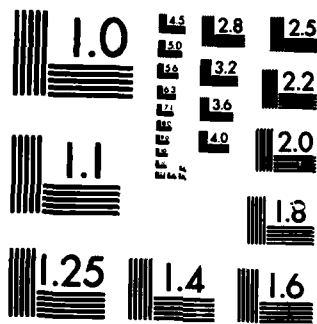
1/2

UNCLASSIFIED

F/G 14/5

NL





MICROCOPY RESOLUTION TEST CHART
NATIONAL BUREAU OF STANDARDS-1963-A

AFOSR-TR- 85-0124

2

Edward L. Ginzton Laboratory
W.W. Hansen Laboratories of Physics
Stanford University
Stanford, California

PHOTOACOUSTIC IMAGING

AD-A150 823

Final Report

for the period

30 June 1982 - 29 June 1984

Grant No. AFOSR-82-0248

Approved for public release;
distribution unlimited.

The views and conclusions contained
in this document are those of the
authors and should not be interpreted
as necessarily representing the
official policies or endorsements,
either expressed or implied, of the
Air Force Office of Scientific Research
or the U.S. Government.

Principal Investigator: Professor C. F. Quate

DTIC FILE COPY

G.L. Report No. 3777

October 1984

DTIC
ELECTE
MAR 05 1985
S D E

85 02 20 060

SECURITY CLASSIFICATION OF THIS PAGE (When Data Entered)

REPORT DOCUMENTATION PAGE		READ INSTRUCTIONS BEFORE COMPLETING FORM
1. REPORT NUMBER AFOSR-TR- 85 - 0124	2. GOVT ACCESSION NO. A150823	3. RECIPIENT'S CATALOG NUMBER
4. TITLE (and Subtitle) PHOTOACOUSTIC IMAGING		5. TYPE OF REPORT & PERIOD COVERED Final Report 30 June 1982-29 June 1984
7. AUTHOR(s) C. C. Williams C. F. Quate		6. PERFORMING ORG. REPORT NUMBER G.L. Report No. 3777
9. PERFORMING ORGANIZATION NAME AND ADDRESS Edward L. Ginzton Laboratory Stanford University Stanford, California 94305		8. CONTRACT OR GRANT NUMBER(s) AFOSR-82-0248
11. CONTROLLING OFFICE NAME AND ADDRESS AFOSR/NE Building 410 Bolling AFB, D.C. 20332		10. PROGRAM ELEMENT, PROJECT, TASK AREA & WORK UNIT NUMBERS 2306/A2 W1102F
14. MONITORING AGENCY NAME & ADDRESS (if different from Controlling Office)		12. REPORT DATE October 1984
		13. NUMBER OF PAGES 99
		15. SECURITY CLASS. (of this report) UNCLASSIFIED
		15a. DECLASSIFICATION/DOWNGRADING SCHEDULE
16. DISTRIBUTION STATEMENT (of this Report) "Approved for public release; distribution unlimited"		
17. DISTRIBUTION STATEMENT (of the abstract entered in Block 20, if different from Report)		
18. SUPPLEMENTARY NOTES		
19. KEY WORDS (Continue on reverse side if necessary and identify by block number) Photoacoustic theory Photothermal probe Thermoacoustic field		
20. ABSTRACT (Continue on reverse side if necessary and identify by block number) This is the final report on the work done in the area of high resolution photo- acoustic and photothermal imaging. It contains recent advances in photo- acoustic and photothermal theory and the experimental demonstration of new techniques. Photoacoustic and photothermal theories have been extended to include the effects of the highly focused optical power sources necessary for high resolution imaging and three high frequency techniques (1 GHz) have been demonstrated and used to characterize the material properties of solids.		

DD FORM 1 JAN 73 1473

EDITION OF 1 NOV 65 IS OBSOLETE

UNCLASSIFIED

SECURITY CLASSIFICATION OF THIS PAGE (When Data Entered)

AIR FORCE OFFICE OF SCIENTIFIC RESEARCH (AFSC)

NOTICE OF TRANSMITTAL TO DTIC

This technical report has been reviewed and is approved for public release under AFMRL 190-12.

Distribution is unlimited.

MATTHEW J. KENNEL

Chief, Technical Information Division

SUMMARY

This is the final report on the work done in the area of high resolution photoacoustic and photothermal imaging. It contains recent advances in photoacoustic and photothermal theory and the experimental demonstration of new techniques. Photoacoustic and photothermal theories have been extended to include the effects of the highly focused optical power sources necessary for high resolution imaging and three high frequency techniques (1 GHz) have been demonstrated and used to characterize the material properties of solids.

The formalism behind photothermal characterization of solids is established under general focusing conditions. An analysis of the frequency dependence of the photothermal response demonstrates that very high frequencies may be employed without loss of sensitivity if highly focused optical beams are used. It is shown that the photothermal signal can be used to directly measure the thermal conductivity of solids on a microscopic scale.

The three dimensional thermoacoustic field equation is derived and discussed. This equation is used to obtain the one dimensional thermoacoustic wave equation. It is shown that an error exists in the traditional one dimensional equation used in photoacoustic theory. A new approach to the solution of the one dimensional problem is presented. It is shown that the far field stress can be related to the thermoacoustic source distribution by a Fourier transform relation under arbitrary acoustic boundary conditions.

Two high resolution photoacoustic techniques have been demonstrated. These techniques involve the use of an acoustic lens for collection of the acoustic power generated by a highly focused optical beam modulated at 1 GHz frequency. Images of gold and laser recrystallized silicon films are presented demonstrating the high resolution and sensitivity of these techniques.

A high resolution photothermal probe has been demonstrated. This optical technique provides a means of photothermal characterization with sub-micrometer resolution and high sensitivity. The theory behind the probe is presented along with the experimental verification. Images of boron implanted silicon are included which demonstrate the resolution and sensitivity of this technique.



CONTENTS

Accession For	
NTIS GRA&I	<input checked="checked" type="checkbox"/>
DTIC TAB	<input type="checkbox"/>
Unannounced	<input type="checkbox"/>
Justification	
By	
Distribution/	
Availability Codes	
Dist	Avail and/or Special
A-1	

1. INTRODUCTION	1
References	7
2. PHOTOTHERMAL RESPONSE	9
2.1 Introduction	9
2.2 Thermal Waves	9
2.3 Characterization of Solids by Photothermal Response	13
2.3.1 One Dimensional Photothermal Response	14
2.3.2 Thermal Frequency Response	17
2.3.3 Dependence upon Thermal Conductivity	18
2.4 Applications of High Frequency Photothermal Characterization	21
References	26
3. THERMOACOUSTIC GENERATION	27
3.1 Introduction	27
3.2 Three Dimensional Thermoacoustic Field Equation	28
3.3 One Dimensional Thermoacoustic Generation	30
3.3.1 Thermoacoustic Wave Equation	30
3.3.2 Solution of the Thermoacoustic Wave Equation	32
3.3.3 Thermoacoustic Generation near an Acoustic Boundary	34
3.4 Thermoacoustic Generation under Spherical Symmetry	36
3.4.1 Thermoacoustic Equation in Spherical Coordinates	38
3.4.2 Temperature Distribution for a Periodic Point Source	39
3.4.3 Spherical Solution	39
3.4.4 Frequency Dependence of Thermoacoustic Coupling	41
References	42

4. HIGH RESOLUTION PHOTOACOUSTIC IMAGING	43
4.1 Introduction	43
4.2 Experimental Description	44
4.3 Sensitivity of the Acoustic Lens as a Photoacoustic Detector	47
4.4 Photoacoustic Imaging Results	48
4.4.1 Laser Recrystallized Silicon Film on a Quartz Substrate	49
4.4.2 Thin Gold Film on a Glass Substrate	54
4.5 Photoacoustic Imaging of a Free Surface	55
References	62
5. HIGH RESOLUTION PHOTOTHERMAL LASER PROBE	63
5.1 Introduction	63
5.2 Derivation of the Bragg Scattering Efficiency	65
5.2.1 Inhomogeneous Wave Equation	67
5.2.2 Derivation of the Photoelastic Relation for an Ideal Gas	68
5.2.3 Calculation of the Acousto-optic Nonlinear Polarization	68
5.2.4 Bragg Scattering Efficiency	70
5.3 Heterodyne Sensitivity	73
5.4 Thermoacoustic Generation of Sound	76
5.5 Photothermal Sensitivity	78
5.6 Acousto-optic Coupling Medium - Figure of Merit	80
5.7 Comparison of Photoacoustic and Photothermal Techniques	81
5.8 Experimental Verification of the Theory	84
5.8.1 Experimental Implementation	84
5.8.2 Frequency Dependence	86
5.8.3 Absolute Sensitivity	88
5.8.4 Dependence on Pressure	90
5.9 Photothermal Imaging of Implanted Silicon	91
5.10 Summary	93
References	94
Appendix	96

FIGURES

1-1. Geometry of photoacoustic and photothermal imaging techniques	3
1-2. Thermal wave imaging techniques	4
2-1. Thermal wave reflection at an interface	12
2-2. Thin film thickness measurement	16
2-3. AC/DC thermal response under various conditions	19
2-4. AC/DC thermal response with variable spot size	20
2-5. AC photothermal dependence upon thermal conductivity	22
2-6. AC photothermal phase dependence upon thermal conductivity	23
3-1. Thermoacoustic generation near an acoustic boundary	35
3-2. One dimensional photoacoustic conversion efficiency	37
4-1. Experimental arrangement for photoacoustic imaging	45
4-2. Modulation depth of a diode laser output at 1 GHz	47
4-3. Photoacoustic sensitivity with an acoustic lens collector	49
4-4. Images of a laser recrystallized silicon film	51
4-5. Images of a laser recrystallized silicon film	52
4-6. Photoacoustic a-trace of a recrystallized silicon film	53
4-7. Images of a 1000 Å gold film on a glass substrate	56
4-8. Comparison of two different photoacoustic geometries	58
4-9. Images of a gold film using gallium as an acoustic coupler	60
5-1. Geometry of the photothermal laser probe	64
5-2. Illustration of the acousto-optic interaction at focus	66
5-3. Collinear Bragg scattering geometry	70
5-4. K-vector matching required for collinear Bragg scattering	72
5-5. Experimental arrangement	85
5-6. Heterodyne detection system	87
5-7. Frequency dependence of Bragg scattering efficiency	89
5-8. Photothermal images of boron implanted silicon	92

TABLES

4-1. Photoacoustic sensitivity with an acoustic lens collector	48
5-1. Comparison of thermoacoustic sources	77
5-2. Experimental conditions of photothermal detection	79
5-3. Comparison of acousto-optic coupling media	81

Chapter 1.

INTRODUCTION

Over the past three decades, a substantial interest in the microscopic properties of materials and material systems has been demonstrated. Many new techniques and tools have been developed for microscopic examination. The use of the scanning electron microscope for elemental analysis on a microscopic scale (microprobe) has provided useful information about the composition of very small systems [1.1]. Work done in the area of transmission electron microscopy has brought the state of the art to the point where individual atoms can be resolved [1.2]. Research in the area of acoustic microscopy has extended the resolution of the water coupled instrument beyond that of optical microscopy [1.3]. In cryogenic liquids, the highest resolution demonstrated to date is approximately 200 angstroms [1.4]. There is hope that further improvement in resolution may be possible. Scanning optical microscopes have been pushed toward their limits using short wavelength laser sources to obtain the highest resolution [1.5]. Recently, a near field approach has extended the resolution of optical microscopy far beyond the diffraction limit [1.6]. Tunneling probes have been successful in imaging the electronic properties of materials with resolution on the atomic scale [1.7]. All of these efforts are manifestations of the interest in the microscopic properties of materials.

Two areas of microscopic imaging which have received attention in recent years are photoacoustic and photothermal imaging [1.8-1.14]. Photothermal imaging is defined to include those techniques which are capable of independently measuring the thermal response of a solid generated by absorption of optical power. The information obtained by these methods does not contain acoustic artefacts which may complicate the interpretation of the data. Photoacoustic techniques, on the other hand, are those which are inherently tied to the coupling of thermal and acoustic waves in the material to be imaged. These techniques can be used to

measure both the thermal and acoustic properties of materials. Each of these areas has been usefully applied to microscopic examination of materials and systems.

Photoacoustic and photothermal imaging are based upon the generation of a periodic thermal distribution in solids by absorption of modulated optical power. See Figure 1-1. The thermal response can be treated as a sum of thermal waves generated by a distribution of point sources in the region of optical absorption. These thermal waves are temperature waves whose characteristics depend upon the thermal properties of the medium in which they are generated. Using highly focused optical beams, this dependence can be exploited to obtain information about the thermal properties of a solid with microscopic resolution.

There are several reasons for the interest in the microscopic thermal properties of materials. In crystalline semiconductors, the thermal conductivity is strongly dependent upon the quality of the crystalline lattice. Perturbations to the crystalline structure caused by defects or dopants can greatly modify the thermal conductivity of the material. The measurement of this thermal parameter is therefore a means of characterizing the crystalline structure as well. Another source of interest is in the area of subsurface characterization. The thermal waves can provide useful information about subsurface structure such as cracks, delaminations and interfaces that cannot be evaluated by other non-destructive techniques. The ability to microscopically measure the thermal properties of materials and non-destructively evaluate subsurface properties provides useful information for materials characterization.

Because thermal waves are highly damped, they are difficult to detect directly. Therefore, various indirect ways for probing the thermal response have been developed. A diagram of the generic classes of these techniques is shown in Figure 1-2. As can be seen from the figure, the techniques can be classified into three general classes, thermo-optic, thermoacoustic, and pyroelectric. Each of these techniques has its advantages and disadvantages, depending upon the sensitivity, simplicity, and spacial resolution required. Most of the techniques are generally useful at modulation frequencies below one hundred kilohertz, where the thermal wavelength

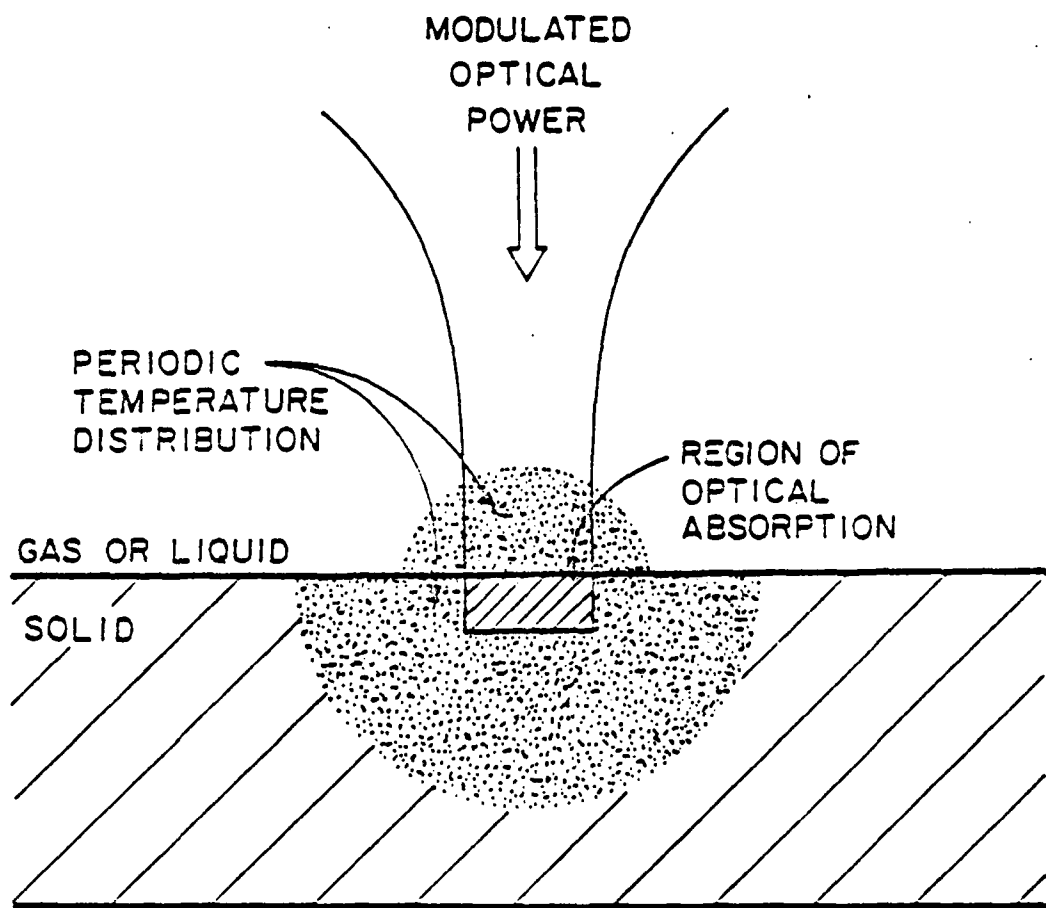


Figure 1-1. The geometrical arrangement generally used in photoacoustic and photothermal imaging. The periodic temperature distribution created by the modulated optical power is shown to extend beyond the region of optical absorption.

THERMAL WAVE IMAGING

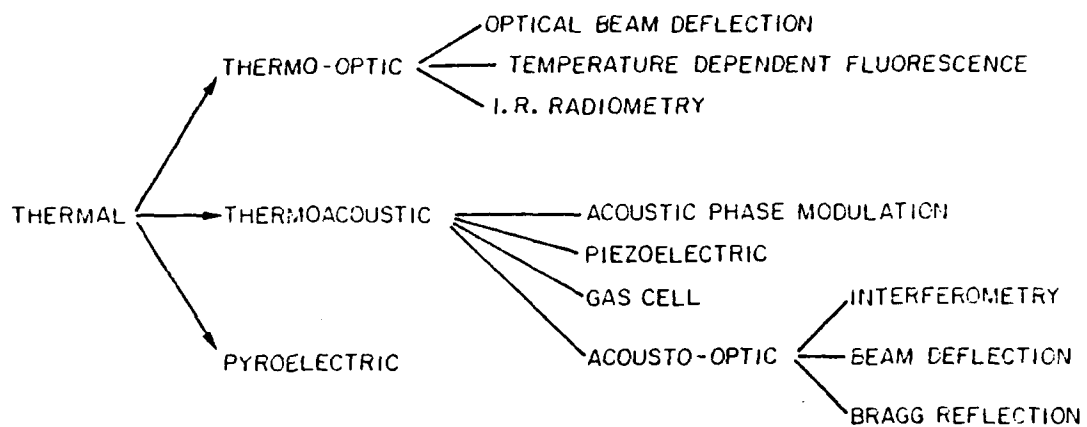


Figure 1-2. Many of the available thermal wave imaging techniques divided into generic classes.

in a semiconductor is greater than 10 microns. Some experiments have been done at 10 MHz frequencies where the thermal wavelength in a semiconductor is greater than 1 micron. The work which will be presented here has been done at frequencies near 1 GHz. The thermal wavelength in these experiments is somewhat greater than 1000 angstroms. Under these conditions, the resolution of the thermal imaging system is essentially limited by the optical spot size.

In order to understand and evaluate the photoacoustic and photothermal experiments that will be presented in the last two chapters of this work, Chapter 2 has been devoted to understanding the photothermal response of materials. This requires an introduction to thermal waves, and an analysis of how the thermal, optical and geometrical properties of materials are related to the photothermal response. A discussion of the applications where photothermal characterization may be useful will then be presented.

Chapter 3 contains an analysis of one and three dimensional thermoacoustic generation. This theory is useful for understanding and comparing the various thermoacoustic techniques, two of which will be presented in Chapter 4. The theory will show that the thermoacoustic conversion efficiency increases with modulation frequency for thermal sources which are small compared to an acoustic wavelength. Also, it will be shown that the existing theory of one dimensional thermoacoustic generation predicts a generation efficiency which is nine times smaller than that predicted by the correct theory.

In Chapter 4, two experiments will be described which involve an acoustic lens as a collector of photoacoustically generated sound. The merits of using a focused acoustic collector will be discussed and the sensitivity of the acoustic lens as a collector of photoacoustically generated sound will be calculated. Images will then be presented demonstrating the sensitivity and resolution of these techniques.

Chapter 5 contains the description of a new photothermal laser probe. The theory behind the probe will be presented and a theoretical sensitivity calculated under reasonable experimental conditions. A figure of merit will be established for evaluation of various acousto-optic coupling media. The

probe will then be compared with two other high resolution techniques. The experimental implementation will be described and verification of the theory will be reported. Finally, photothermal images of boron implanted silicon will be presented demonstrating the sensitivity and resolution of this technique.

References for Chapter 1

- [1.1] Raymond Castaing, "Electron Probe Microanalysis," *Advances in Electronics and Electron Physics*, L. Marton, ed., New York: Academic Press, 1960, p. 317.
- [1.2] Fernando A. Ponce, "Fault-free silicon at the silicon/sapphire interface," *Appl. Phys. Lett.* **41**, 371 (1982).
- [1.3] B. Hadimioglu and C.F. Quate, "Water acoustic microscopy at suboptical wavelengths," *Appl. Phys. Lett.* **43**, 1006 (1983).
- [1.4] B. Hadimioglu and J.S. Foster, "Advances in superfluid helium acoustic microscopy," (Submitted to Journal of Applied Physics).
- [1.5] G.J. Brakenhoff, J.S. Binnerts and C.L. Woldringh, "Developments in High Resolution Confocal Scanning Light Microscopy," *Scanned Image Microscopy*, Eric A. Ash, ed., London: Academic Press, 1980, p. 183.
- [1.6] D.W. Pohl, W. Denk, and M. Lanz, "Optical stethoscopy: Image recording with resolution $\lambda/20$," *Appl. Phys. Lett.* **44**, 651 (1984).
- [1.7] G. Binnig, H. Rohrer, Ch. Gerber, and E. Weibel, "7 X 7 Reconstruction on Si(111) Resolved in Real Space," *Phys. Rev. Lett.* **50**, 120 (1983).
- [1.8] Y.H. Wong, R.L. Thomas and G.F. Hawkins, "Surface and subsurface structure of solids by laser photoacoustic spectroscopy," *Appl. Phys. Lett.* **32**, 538 (1978).
- [1.9] H. K. Wickramasinghe, R. Bray, V. Jipson, C. Quate and J. R. Salcedo, "Photoacoustics on a Microscopic Scale," *Appl. Phys. Lett.* **33**, 923 (1978).
- [1.10] Allan Rosencwaig and G. Busse, "High-resolution photoacoustic thermal-wave microscopy," *Appl. Phys. Lett.* **36**, 725 (1980).
- [1.11] S. Ameri, E. A. Ash, V. Neuman, C. R. Petts, "Photo-displacement Imaging", *Electron Lett.* **17**, 337 (1981).
- [1.12] J.C. Murphy and L.C. Aamodt, "Optically detected photothermal imaging," *Appl. Phys. Lett.* **38**, 196 (1981).

- [1.13] Marjorie A. Olmstead and Nabil M. Amer, "A new probe of the optical properties of surfaces," *J. Vac. Sci. Technol. B* **1**, 751 (1983).
- [1.14] C.C. Williams, "High resolution photothermal laser probe," (accepted for publication in *Appl. Phys. Lett.*).

Chapter 2.

PHOTOTHERMAL RESPONSE OF MATERIALS

2.1 Introduction

Both photoacoustic and photothermal imaging have their basis in the conversion of modulated optical power into a periodic temperature distribution in a solid. The thermal response depends upon several parameters which include the characteristics of the heating beam i.e. modulation frequency and spot diameter, and the material properties and geometry of the absorbing system i.e. optical absorption constant, thermal conductivity, density, specific heat and film thickness. An understanding of these factors makes possible the characterization of solids by experimental measurement of the photothermal response.

In this chapter, the photothermal response of solids will be examined. Since this response can be treated most clearly using a thermal wave (or Green's function) approach, a discussion of thermal waves will be presented. The dependence of the thermal response upon the modulation frequency, the optical and thermal properties of the solid, and geometry will then be examined. In the final section, the possibilities for useful application of these principles will be discussed.

2.2 Thermal Waves

The thermal response of a system is governed by the inhomogeneous thermal diffusion equation shown below [2.1].

$$\nabla^2 \theta - \frac{1}{\kappa} \frac{\partial \theta}{\partial t} = \frac{-1}{K} A(\vec{r}, t) \quad (2.1)$$

The variable θ is the temperature, κ is the thermal diffusivity, K is the thermal conductivity, and $A(\vec{r}, t)$ is the power per volume released in the medium. If the

source function $A(\vec{r}, t)$ is harmonic,

$$A(\vec{r}, t) = A(\vec{r})e^{j\omega t} \quad (2.2)$$

the diffusion equation becomes

$$\nabla^2 \theta + k_t^2 \theta = \frac{-1}{K} A(\vec{r}), \quad (2.3)$$

where

$$k_t = \left(\frac{\omega}{2\kappa} \right)^{\frac{1}{2}} (1 + j). \quad (2.4)$$

This equation looks like the Helmholtz equation, encountered in electromagnetics. However, the term k_t^2 is complex in the thermal case, whereas in the electromagnetic case it is real.

The Green's function for this equation can be obtained if we substitute a delta function for the spacial dependence of the source function.

$$A(\vec{r}, t) = \delta(\vec{r} - \vec{r}_o) e^{j\omega t} \quad (2.5)$$

With this as the source term, the solution is given by [2.2]

$$G_\theta(\vec{r}|\vec{r}_o; \omega) = \frac{1}{4\pi K |\vec{r} - \vec{r}_o|} e^{-k_t |\vec{r} - \vec{r}_o|} e^{j\omega t}. \quad (2.6)$$

This is the Green's function solution to the thermal diffusion equation with a harmonic source. This solution has been called a thermal wave. One of the advantages of a harmonically varying thermal source when compared to a pulsed source is that thermal waves have a fixed velocity and wavelength. Under these circumstances, a phase delay can be related to a distance or a variation in the thermal properties of the medium. In contrast, when a pulse of heat is generated, all the Fourier components of the heat pulse propagate at different velocities, and the pulse shape changes rapidly with the diffusion of heat to the surrounding areas. Therefore, no unique velocity can be attributed to the transfer of heat.

The periodic thermal response at any point due to a spacially distributed source can be obtained by integrating the product of the source function and the Green's

function over the volume where the source is finite.

$$\theta(\vec{r}, \omega) = \int_V G_\theta(\vec{r}|\vec{r}_o; \omega) A(\vec{r}_o) dV_o \quad (2.7)$$

There are several interesting properties of thermal waves. First, these waves have k-vectors which have equal real and imaginary parts. They are therefore very highly damped. Second, the thermal k-vector is proportional to the square root of the frequency. By contrast, in the frequency range of interest, the acoustic k-vector is proportional to the frequency. This results in a change in the ratio of the thermal to acoustic wavelength as the frequency is changed. At low frequencies, the thermal wavelength is very small compared to the acoustic wavelength. At high frequencies, the thermal wavelength begins to approach the wavelength of sound. However, at frequencies where the thermal wavelength approaches the acoustic wavelength, the thermal waves begin to lose their diffusive character. This is true because equal wavelength implies equal velocity. If the velocity of the thermal wave approaches that of sound, it cannot be diffusive. Fortunately, for most materials, this occurs at frequencies near 100 GHz, far from the region of interest (1 GHz).

$$\frac{\lambda_t}{\lambda_a} = \frac{(2\kappa\omega)^{\frac{1}{2}}}{V_a} = \left(\frac{f}{f_0}\right)^{\frac{1}{2}} \quad (2.8)$$

$$f_0 = \frac{V_a^2}{4\pi\kappa} \approx 10^{11} \quad (2.9)$$

Third, materials can be characterized by a thermal impedance. The thermal impedance Z_i is given by the ratio of the temperature to the heat flux for a traveling thermal plane wave in medium i . This thermal impedance is related to the material properties by the following relation.

$$Z_i = \left(\frac{1}{\omega K_i \rho_i C_i}\right)^{\frac{1}{2}} \left(\frac{1-j}{\sqrt{2}}\right) \quad (2.10)$$

See Figure 2-1. Using this impedance, a thermal reflection and transmission coefficient can be obtained using the following relation.

$$r = \frac{(Z_2 - Z_1)}{(Z_2 + Z_1)} \quad (2.11)$$

THERMAL WAVE REFLECTION

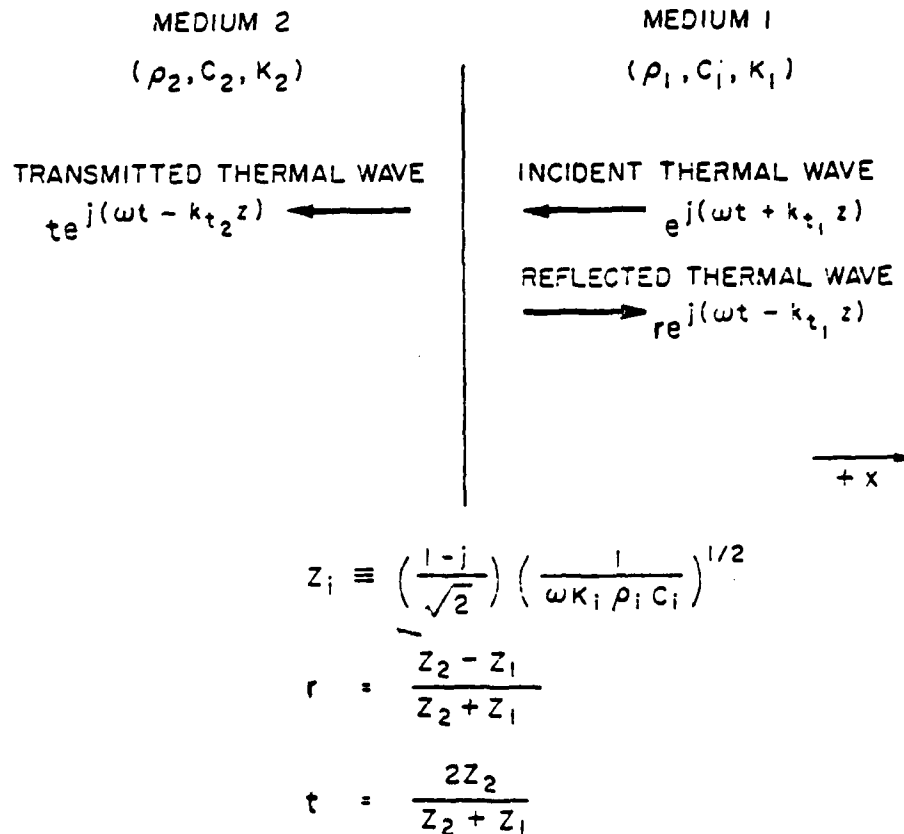


Figure 2-1. Illustration of the reflection and transmission of a thermal plane wave that takes place at an interface between two media of different thermal impedance. The thermal impedance of medium i depends upon the radian frequency ω , the thermal conductivity K_i , the density ρ_i , and the specific heat C_i .

Because the generation and propagation of thermal waves depends upon the geometrical, thermal and optical properties of the medium in which they exist, a measurement of the thermal response makes possible characterization of the medium. In the next section, the dependence of the thermal response upon several parameters will be examined. These results demonstrate that information about material properties can be extracted from the photothermal response.

2.3 Characterization of Solids by Photothermal Response

The photothermal response of a solid depends upon many different geometric and material parameters. The important geometric parameters are the diameter of the optical spot, the thickness and geometry of the materials, and the ratio of these parameters to the thermal wavelength. The material parameters which effect the photothermal response are the thermal conductivity, specific heat, optical absorption coefficient and the thermal impedance. In order to extract useful information about a solid from a photothermal measurement, the dependence of the thermal response upon these parameters must be well understood. In this section, these parameters and their effect on the thermal response will be discussed.

When the optical spot size is very large compared with a thermal wavelength, the photothermal response can be treated one dimensionally. The results from the one dimensional theory will be summarized in the next section. When the optical spot size is smaller than or on the order of the thermal wavelength, a three dimensional theory must be used. The three dimensional analysis has been done using the numerical routine found in the Appendix. The results of these calculations are contained in the sections which follow. Included in this analysis is the dependence of the thermal response upon frequency, optical absorption depth, optical spot size, and thermal conductivity. Finally, a discussion of the application of this characterization capability will be presented.

2.3.1 One Dimensional Photothermal Response

When the optical spot size is many thermal wavelengths in diameter, the ac temperature at the surface of the solid due to the absorption of the modulated light can be treated with a one dimensional theory. Most of this theory has been extensively described by Rosensweig and Gersho [2.3] and therefore will only be summarized here. There are five cases of interest. The model used here consists of three regions: a vacuum, an absorbing layer, and an infinite backing. Modulated light, incident through the vacuum, periodically heats the absorbing layer. This region is characterized by a thermal conductivity K , density ρ , specific heat C , optical absorption coefficient β , and thickness L . The infinite backing is characterized by a thermal conductivity, density and specific heat. The resulting harmonic temperature response at the surface of the absorbing layer is calculated for an optical intensity modulation I_0 at a radian frequency ω . The thermal k-vector is given by k_t . When the thickness of the absorbing layer is much less than the thermal wavelength, it is called thermally thin. If its thickness is much greater than the thermal wavelength, it is called thermally thick. Likewise with the optical absorption depth.

Case1 - Thermally thick, optically thin

In this case, the magnitude of the sinusoidal temperature rise at the surface of the absorbing layer is proportional to the optical attenuation constant, and inversely proportional to the modulation frequency, density and the heat capacity.

$$\theta = \frac{-j\beta I_0}{2\omega\rho C} \quad (2.12)$$

Case2 - Thermally thick, optically thick, for β much greater than k_t

The temperature in this case is inversely proportional to the square root of the thermal conductivity, density, heat capacity, and frequency. Note that this is the case treated by White [2.4].

$$\theta = \frac{I_0}{2\sqrt{K\rho C\omega}} \left(\frac{1+j}{\sqrt{2}} \right) \quad (2.13)$$

Case3 - Thermally thick, optically thick, for k_T much greater than β

The temperature in this case is proportional to the optical absorption constant, and inversely proportional to the frequency, density and heat capacity.

$$\theta = \frac{-j\beta I_0}{2\omega\rho C} \quad (2.14)$$

Case4 - Thermally thin, optically thick, for β much greater than k_T

In this case, the temperature is inversely proportional to the square root of the thermal conductivity, density, heat capacity and frequency. There is a complicated dependence on the thermal wave reflections at the interface between the absorbing layer and the substrate.

$$\theta = \frac{-I_0(1-j)\beta}{2\sqrt{2}\sqrt{K\rho C\omega}} \left(\frac{e^{\sigma L} + re^{-\sigma L}}{e^{\sigma L} + re^{-\sigma L}} \right) \quad (2.15)$$

$$\sigma = \left(\frac{\omega}{2\kappa} \right)^{\frac{1}{2}} (1+j) \quad (2.16)$$

The thermal wave reflection coefficient at the interface is given by r .

Case5 - Optically transparent film on an absorbing substrate

If the harmonic temperature rise at the interface between the transparent film and the absorbing substrate is given by θ_i , the harmonic temperature at the surface of the film is proportional to an exponential with an exponent which is the product of the thermal k-vector and the thickness of the film. See Figure 2-2.

$$\theta = \theta_i e^{-k_t L} \quad (2.17)$$

There are several interesting points that can be made with the results presented above. First, it is apparent that if one desires a sensitivity to the thermal conductivity of a material, the optical absorption depth should be short compared to the thermal wavelength ($\beta \gg k_t$). This seems intuitive since no thermal diffusion takes place in a region which is uniformly heated. Second, the product of density and specific heat seen in many of the expressions above does not contain very much useful information, because at room temperature this product varies little

THIN FILM THICKNESS MEASUREMENT

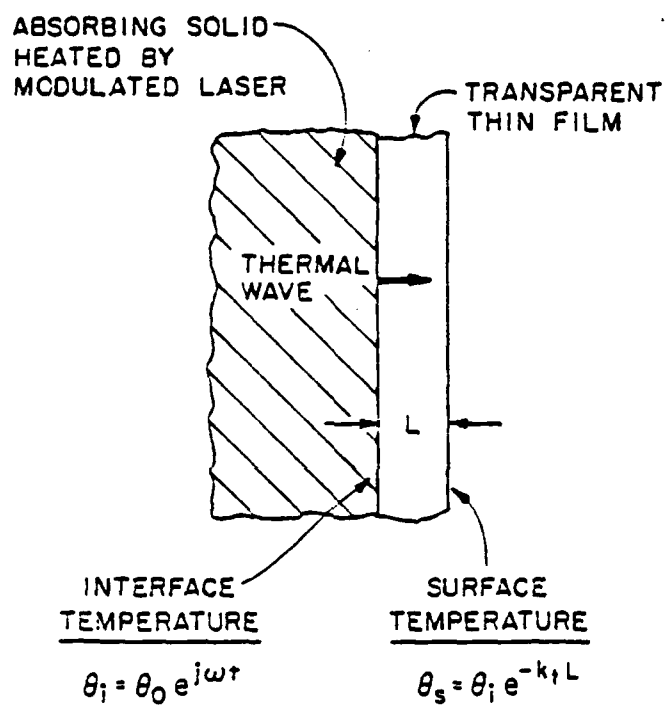


Figure 2-2. Illustration of how the surface temperature of a film depends upon its thickness L and the thermal k -vector k_t when the substrate upon which it sits is harmonically heated.

from material to material. Third, Case 4 indicates that the thermal properties of a subsurface boundary between two materials may be evaluated by measuring the reflected thermal waves from the interface. High frequency thermal waves are uniquely suited to such subsurface characterization. Fourth, Case 5 indicates that the measurement of film thickness may be possible when the film is optically transparent. Under this circumstance, any spacial variation of the thickness could be determined by either an amplitude or phase measurement of the temperature at the surface of the film.

2.3.2 Thermal Frequency Response

The experimental work presented in chapters 4 and 5 has been done with optical power modulated at frequencies near 1 GHz. This raises the question of whether the material can thermally respond at such a high frequency. In this section, the results of an analysis of thermal frequency response will be presented. The essence of this analysis is that when the dimensions of the thermal source are smaller than or equal to the thermal wavelength, the thermal frequency response will not limit the sensitivity of the photothermal system. Intuitively this result can be understood by considering the fact that the heat flux away from the thermal source region is proportional to the temperature gradient. When the source is very small, the gradient becomes very large, and the flux can be enormous. The large heat flux makes possible a rapid change in the temperature. This lack of thermal inertia is equivalent to a frequency response which extends out to very high frequencies.

The thermal frequency response of a system is important because the sensitivity of a photothermal technique is generally limited only by the maximum allowable optical power that can be deposited non-destructively in the sample. Since negative heat cannot be supplied, there is always as much dc or average heating as there is ac heating. In general, the ac response is less than the dc response. Since the photothermal signal is proportional to the ac temperature response, one would like to have an ac response that is near that of the dc response so that the upper bound on average heating does not limit the size of the ac photothermal signal.

To examine the thermal frequency response, the program listed in the Appendix was written. The program calculates the ac and dc temperature rise at the surface of a semi-infinite solid when heated by a modulated Gaussian beam of light. The variables include the beam width, optical absorption depth, and modulation frequency, as well as the thermal conductivity, density, and specific heat of the solid.

In Figure 2-3, the ratio of the ac to dc response is plotted as a function of two parameters, the ratio of the thermal wavelength to optical absorption depth and the ratio of the thermal wavelength to the optical spot radius. The plot indicates that the thermal source should have dimensions smaller than or equal to the thermal wavelength if the ac response is to be near the dc response.

Figure 2-4 shows the ac/dc response ratio for 1 GHz modulation frequency in silicon as a function of optical spot size. As can be seen from the plot, the ac response can be near the dc response at a frequency of 1 GHz, if the optical beam is tightly focused to a submicron spot. Practically, this means that if the silicon can tolerate an average temperature of 20 degrees above the ambient, then a 5 degree harmonic response at a frequency of 1 GHz can be obtained if a submicron optical spot is used. In the next section, it will become clear that having a thermal source which is smaller than or equal to the thermal wavelength is important for another reason.

2.3.3 Dependence upon Thermal Conductivity

Using the program found in the Appendix, the dependence of the harmonic thermal response on thermal conductivity was calculated for several optical spot diameters. The calculation was done using the material values of silicon at a modulation frequency of 1 GHz. The value for the thermal conductivity of silicon was varied between 25 and 500 W/m²K. The ac thermal response for each spot size was calculated and normalized to show the increasing sensitivity to changes in thermal conductivity with decreasing spot size. Since many of the photothermal techniques can measure both the amplitude and phase of the photothermal response,

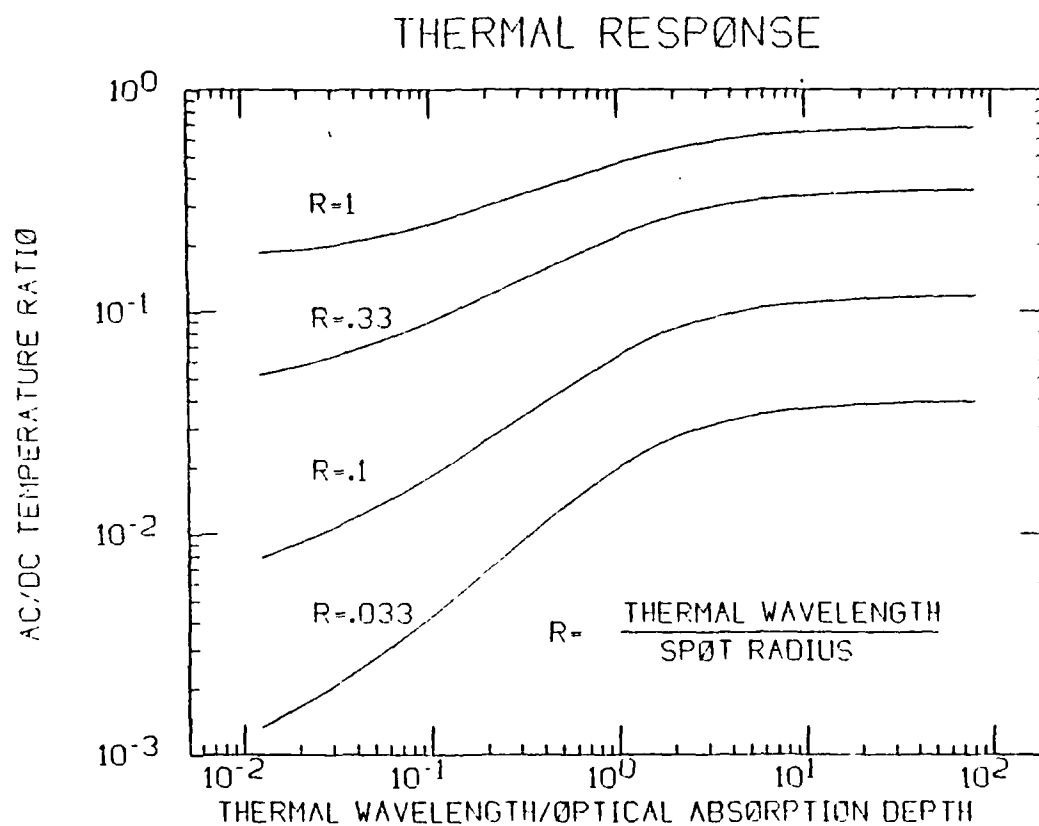


Figure 2-3. The ac to dc temperature ratio at the surface of a solid created by the absorption of a harmonically modulated Gaussian beam. The ratio is plotted against two parameters, the ratio of thermal wavelength to optical spot radius and the ratio of thermal wavelength to optical absorption depth.

THERMAL RESPONSE OF SILICON

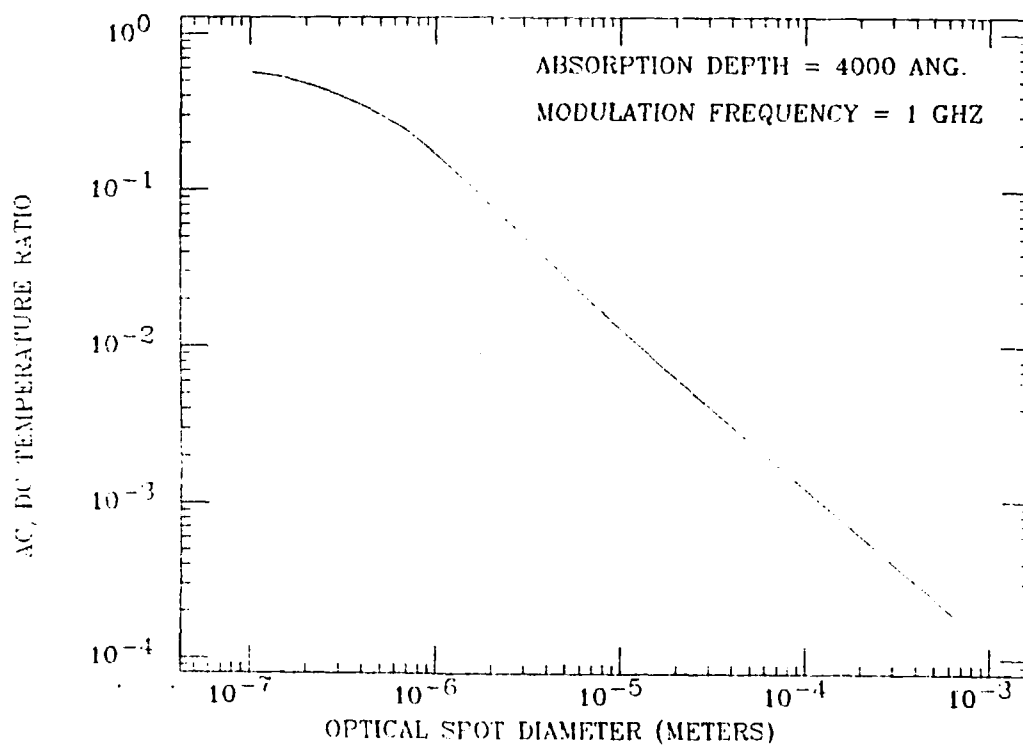


Figure 2-4. The ratio of the ac to dc temperature at the surface of silicon due to the absorption of a Gaussian beam of variable spot diameter modulated at a frequency of 1 GHz.

these were plotted independently. The dependence of the amplitude on thermal conductivity is shown in Figure 2-5. The dependence of the phase is shown in Figure 2-6.

The plots clearly show that there is another reason for focusing the optical spot as tightly as possible. When the thermal source becomes large compared to the thermal wavelength, the dependence of the harmonic response on the thermal conductivity goes to zero. When the thermal source is smaller than or of the same dimension as the thermal wavelength, the photothermal signal can be used to directly measure the thermal conductivity.

2.4 Applications of High Frequency Photothermal Characterization

In the previous sections, it has been shown that the photothermal response can be used to measure the geometrical and thermal properties of materials. In particular, it was shown that the photothermal response depends upon the thermal conductivity of the material under evaluation. In this section, the areas where such information could be useful will be examined.

Because the thermal conductivity is a strong function of the crystallinity of a semiconducting solid, photothermal characterization could be used to evaluate the crystalline defect density in these materials. For example, the thermal conductivity of single crystal silicon at room temperature is near $150 \text{ W/m}^\circ \text{K}$ [2.5]. Amorphous silicon has a thermal conductivity of approximately $2 \text{ W/m}^\circ \text{K}$ [2.6]. This is a change of almost two orders of magnitude. When a crystalline material is implanted with high energy dopants, the lattice can be driven toward an amorphous state. Under such circumstances, high frequency photothermal analysis could provide a measure of the resultant crystallinity with high spacial resolution.

When dopants are diffused into a crystalline semiconductor, the thermal conductivity is changed. Photothermal measurement could also provide a measure of the dopant distribution and density. Holland [2.7] has shown that this change is small at room temperature when the dopant density is less than $10^{18}/\text{cm}^3$. Therefore, at room temperature, only a very large dopant density can

THERMAL RESPONSE OF SILICON

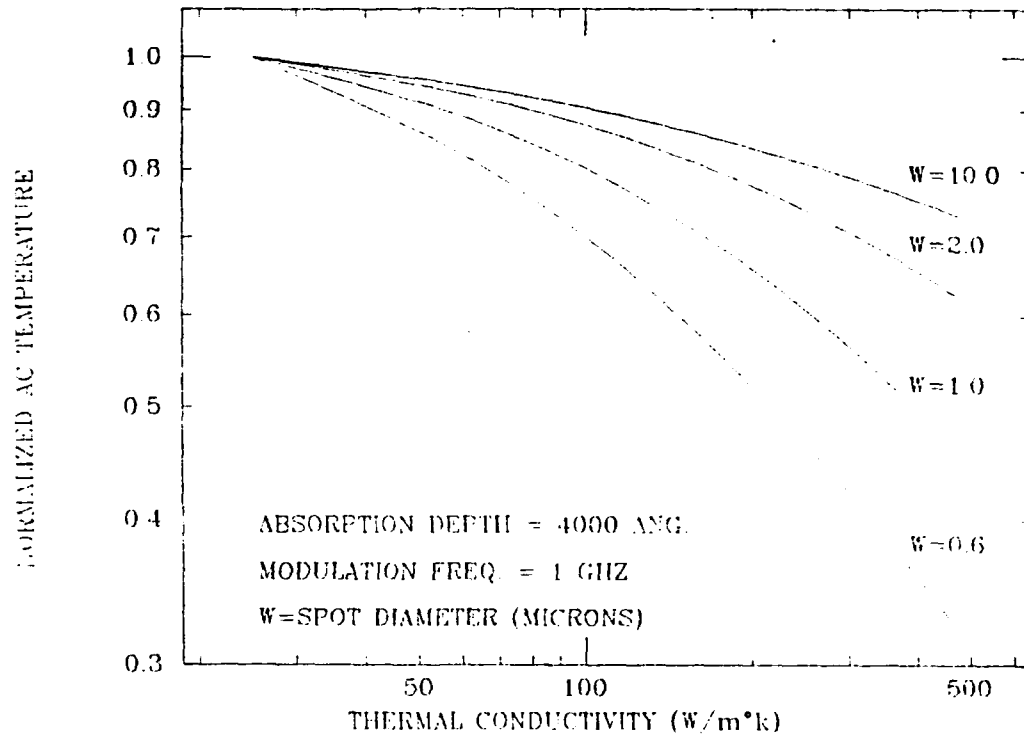


Figure 2-5. This plot shows the dependence of the ac photothermal response on the thermal conductivity for several spot diameters using the material values of silicon. The plot indicates that the dependence on the thermal conductivity increases with decreasing spot size.

THERMAL RESPONSE OF SILICON

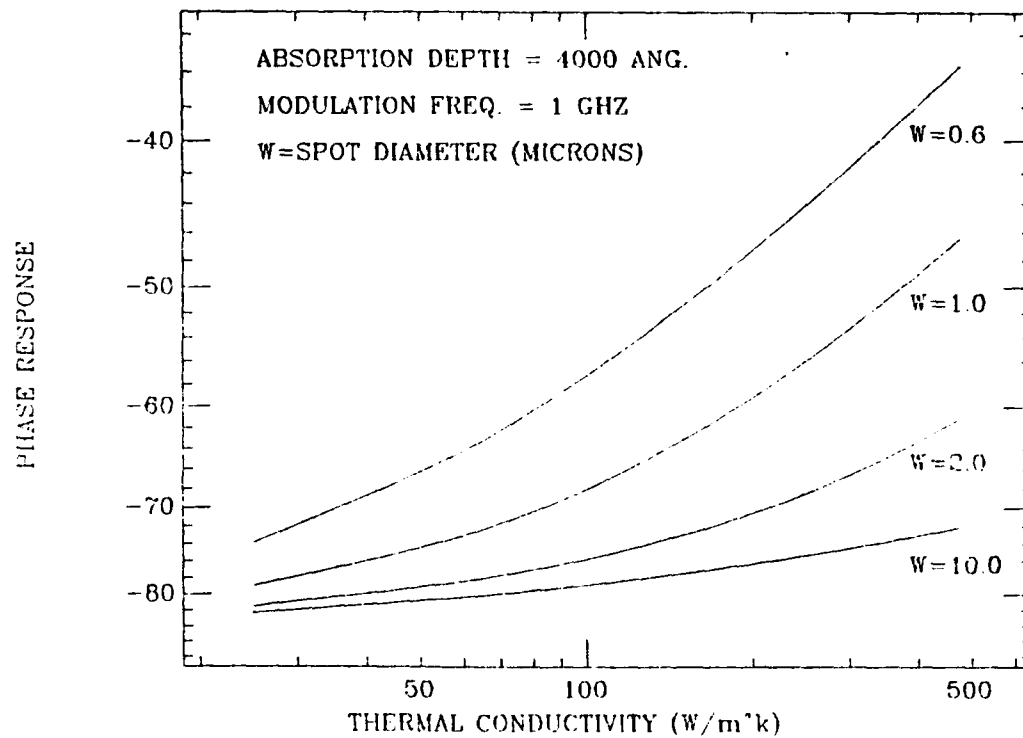


Figure 2-6. This plot shows the dependence of the photothermal phase upon the thermal conductivity for various spot diameters using the material values of silicon. The variation of the phase with changing thermal conductivity is greatest for small spot diameters.

be detected. However, at temperatures below 100 ° K, the thermal properties depend more strongly on dopant or defect densities [2.8]. At these temperatures, the photothermal response could provide a very sensitive measure of dopant densities much less than $10^{18}/\text{cm}^3$ with high spacial resolution.

In anisotropic crystalline solids, the magnitude of the thermal conductivity depends upon the direction of the diffusion relative to the primary crystalline axes. This fact manifests itself when a photothermal image of a polycrystalline material with anisotropic crystallites is obtained. When the crystallites are oriented at different angles with respect to the focused beam, the photothermal response varies. This response can be used to identify and map the various crystalline orientations in a polycrystalline material.

As was shown in section 2.3, another application for high frequency thermal waves is the evaluation of subsurface interfaces. Since thermal waves can propagate through optically opaque materials, they provide a unique tool for subsurface analysis. In a layered system, a variation of the thermal properties of the materials at an interface will modify the reflection coefficient seen by the incident thermal waves. They can therefore be used to probe the material properties at the interface. An example of one interesting case for study is the interaction that takes place when gold is deposited upon gallium arsenide [2.9]. At the interface between these materials, a time dependent chemistry takes place which can modify the properties of the system. Thermal waves analysis could provide useful information about the spacial and temporal development of such chemistry.

Also shown in section 2.3 is the fact that the thickness and thermal properties of a thin film can be determined by photothermal measurement. At high frequencies, the thermal wavelength in insulators can be less than 200 Å. This would make possible the measurement of thin films with thicknesses less than 100 Å with micron lateral resolution and good precision.

Finally, the photothermal technique can be used to probe the adhesion properties of thin films or layered systems. The advantage of using a high frequency photothermal technique over other methods is that the thermal wavelength can be

short compared to optical or acoustic wavelengths. When a separation between two media exists, the reflectivity due to the separation will be proportional the spacing to wavelength ratio. With the short thermal wavelengths, very small spacings can be detected.

References for Chapter 2

- [2.1] H.S. Carslaw and J.C. Jaeger, *Conduction of Heat in Solids*, Oxford: Oxford University Press, 1980, p. 10.
- [2.2] H.S. Carslaw and J.C. Jaeger, *Conduction of Heat in Solids*, Oxford: Oxford University Press, 1980, p. 263.
- [2.3] Allan Rosenzweig and Allen Gersho, "Theory of the photoacoustic effect with solids," *J. Appl. Phys.* **47**, 64 (1976).
- [2.4] R.M. White, "Generation of Elastic Waves by Transient Surface Heating," *J. Appl. Phys.* **34**, 3559 (1963).
- [2.5] Arto Lietoila, *Laser Processing of High Dose Ion Implanted Si: The Solid Phase Regime*, Ph.D. Thesis, Stanford University, 1981, p. 9.
- [2.6] Arto Lietoila, *Laser Processing of High Dose Ion Implanted Si: The Solid Phase Regime*, Ph.D. Thesis, Stanford University, 1981, p. 15.
- [2.7] S. Holland and R.M. White, "Concentration Dependence of Thermal-Wave Contrast for Dopants in Silicon," *1983 Proc. Ultrasonics Symposium*, Atlanta, Georgia, 1983, p. 681.
- [2.8] Glen A. Slack, "Thermal Conductivity of Pure and Impure Silicon, Silicon Carbide, and Diamond," *J. Appl. Phys.* **35**, 3460 (1964).
- [2.9] William E. Spicer, private communication.

Chapter 3.

Thermoacoustic Generation

3.1 Introduction

The photothermal response described in the previous chapter is difficult to directly detect due to the highly damped character of the thermal waves. Fortunately, this harmonic thermal response couples to an acoustic wave through the periodic expansion which also takes place in a medium when its temperature is locally modulated. The thermoacoustically generated sound is relatively undamped and may propagate away from the source region, carrying with it information about the local thermal and acoustic properties of the solid. In order to extract this information from the acoustic power radiated from the source region, a thorough understanding of thermoacoustic coupling is required. In this chapter, the three dimensional thermoacoustic field equation will be derived and solutions for one and three dimensional generation will be presented.

In the first section, the thermoacoustic field equation will be derived for an infinite isotropic solid with a spatially non-uniform temperature distribution. This equation will then be used to derive the one dimensional thermoacoustic wave equation, and it will be shown that an error exists in the traditional one dimensional thermoacoustic theory in solids as presented by White [3.1]. The new theory predicts that the thermoacoustic generation efficiency is nine times that predicted by the previous theory. Using a Green's function approach, the one dimensional problem will be solved for arbitrary acoustic boundary conditions. This approach will make the understanding of the thermoacoustic coupling efficiency at an acoustic boundary very straight forward.

Finally, the three dimensional thermoacoustic field equation will be used to obtain a solution for a spherically symmetric thermal distribution in an infinite isotropic solid. The implications of this theory will be discussed, and a comparison made with the predictions of one dimensional theory.

3.2 Three Dimensional Thermoacoustic Field Equation

The stress-strain relationship for an isotropic solid with uniform temperature is given by

$$\underline{T} = [c] \underline{S}, \quad (3.1)$$

where \underline{T} is the acoustic stress tensor, $[c]$ is the stiffness tensor, and \underline{S} is the strain tensor. The presence of non-uniform temperature produces an additional strain which does not contribute to the stress [3.2]. If the following definitions are made,

\underline{S}_θ = strain due to non-uniform temperature

\underline{S}_a = strain due to acoustic forces (no temperature)

$\underline{S} = \underline{S}_\theta + \underline{S}_a$ = total strain

then the stress-strain relation for an isotropic solid with a non-uniform temperature distribution is given by

$$\underline{T} = [c] \underline{S}_a = [c](\underline{S} - \underline{S}_\theta) = [c] \underline{S} - [c] \underline{S}_\theta. \quad (3.2)$$

The strain due to the non-uniform temperature is purely dilational. In contracted notation [3.3], it is given by

$$\underline{S}_\theta = \alpha_s \theta \begin{pmatrix} 1 \\ 1 \\ 1 \\ 0 \\ 0 \\ 0 \end{pmatrix}, \quad (3.3)$$

where α_s is the linear coefficient of expansion and θ is the temperature difference between actual temperature and some reference temperature of the body. Taking the product of the isotropic stiffness tensor and the thermal strain tensor, we obtain

$$[c] \underline{S}_\theta = (c_{11} + 2c_{12}) \alpha_s \theta \begin{pmatrix} 1 \\ 1 \\ 1 \\ 0 \\ 0 \\ 0 \end{pmatrix} = 3B \alpha_s \theta \begin{pmatrix} 1 \\ 1 \\ 1 \\ 0 \\ 0 \\ 0 \end{pmatrix}, \quad (3.4)$$

where B is the bulk modulus. Under these conditions, the stress-strain relation is given by

$$\mathcal{I} = [c]\mathcal{E} - 3B\alpha_s\theta \begin{pmatrix} 1 \\ 1 \\ 1 \\ 0 \\ 0 \\ 0 \end{pmatrix}. \quad (3.5)$$

This relation is called the Duhamel-Neumann law [3.4]. This expression indicates that the temperature distribution cannot be looked at as a simple generator of strain. In fact, the stress and strain variables are symmetrically related to the non-uniform temperature. The relative amount of strain or stress generated by a thermal source is determined by boundary and symmetry conditions, as will be discussed later.

To obtain the acoustic field equation, the divergence of the stress must be equated to the density-acceleration product at each point.

$$\nabla \cdot \mathcal{I} = \rho \frac{\partial \vec{v}}{\partial t} \quad (3.6)$$

After quite some algebra, the result is

$$\nabla \cdot \mathcal{I} = (\lambda + 2\mu)\nabla(\nabla \cdot \vec{u}) - \mu(\nabla \times \nabla \times \vec{u}) - 3B\alpha_s\nabla\theta. \quad (3.7)$$

In an infinite medium, the thermoacoustic source couples only to displacements which are dilational. Therefore any displacement which is rotational need not be considered. The curl of the displacement can therefore be set equal to zero. This also means that the gradient of the divergence of the displacement is just the Laplacian of the displacement. Under these conditions, the vector displacement equation with a thermal source term becomes (for dilational displacements)

$$(\lambda + 2\mu)\nabla^2 \vec{u} = \rho \frac{\partial^2 \vec{u}}{\partial t^2} + 3B\alpha_s\nabla\theta. \quad (3.8)$$

This is the thermoacoustic field equation for an infinite isotropic solid with a non-uniform temperature distribution.

3.3 One Dimensional Thermoacoustic Generation

In this section, the one dimensional thermoacoustic wave equation will be obtained by substituting into equation (3.8) a harmonic thermal source which varies in only one dimension of space. The results obtained differ from those presented by White [3.1] in his classic paper on thermoacoustic generation. The source of the discrepancy will be examined. After establishing the one dimensional thermoacoustic equation, a Green's function approach will be used to find the solution. This approach will clarify how the thermal distribution couples to an acoustic wave. This analysis will also show that the generated far field strain in the solid is proportional to the Fourier transform of the thermal distribution evaluated at the value of the acoustic k-vector. This analysis is applicable to an arbitrary one dimensional acoustic boundary condition. The frequency dependence of the one dimensional thermoacoustic conversion efficiency will also be discussed.

3.3.1 Thermoacoustic Wave Equation

The one dimensional thermoacoustic field equation can be obtained by substituting a one dimensional thermal distribution into the three dimensional thermoacoustic equation.

$$\theta(x, y, z) = \theta(z) \quad (3.9)$$

If the gradient of this temperature distribution is substituted into equation (3.8), three scalar equations are obtained. The two equations in the x and y coordinates do not have source terms and therefore can be neglected. The equation in the z coordinate is given by

$$(\lambda + 2\mu) \frac{\partial^2 u_z}{\partial z^2} - \rho \frac{\partial^2 u_z}{\partial t^2} = 3B\alpha_s \frac{\partial \theta}{\partial z}. \quad (3.10)$$

Under temporally harmonic conditions, the equation becomes

$$\frac{\partial^2 u_z}{\partial z^2} + k_a^2 u_z = \frac{3B\alpha_s}{c_{11}} \frac{\partial \theta}{\partial z}. \quad (3.11)$$

This is the one dimensional thermoacoustic wave equation.

The thermoacoustic wave equation obtained by White is identical to equation (3.11) above, except that the thermal source term is a factor of three smaller. The discrepancy between this result and that of White can be understood if a comparison is made between the Duhamel-Neumann law and the relation which was used to derive White's result. The Duhamel-Neumann law provides a relation between the stress T_3 , the strain components S_1 , S_2 , and S_3 , and the temperature θ .

$$T_3 = c_{11}S_3 + c_{12}(S_1 + S_2) - 3B\alpha_s\theta \quad (3.12)$$

Under one dimensional symmetry in an infinite medium, the strain in the lateral dimensions (S_1 and S_2) must be zero. This is true because there are no boundaries or temperature gradients to break the lateral symmetry. Thus, the individual elements of the solid see uniform compressional forces from the lateral directions, and the net lateral displacement is zero.

$$S_1 = S_2 = 0 \quad (3.13)$$

Substituting this condition into equation (3.12) provides the following relation between the stress, strain and temperature under one dimensional symmetry,

$$T_3 = (\lambda + 2\mu)S_3 - 3B\alpha_s\theta \quad (3.14)$$

where $(\lambda + 2\mu) = c_{11}$. White derived the thermoacoustic field equation using the following relation.

$$T_3 = (\lambda + 2\mu)S_3 - B\alpha_s\theta \quad (3.15)$$

Comparing these two equations, it is apparent that there is a factor of three missing from the relation used by White. A look at the reference [3.2] sighted by White as the source of equation (3.15) makes it clear that an error was made in transferring this relation from the reference. Analysis done by Bray [3.5] and Rosencwaig [3.6] also contain the same error. Opsal [3.7] uses the correct one dimensional thermoacoustic field equation (3.11) without any comment or derivation.

Since equation (3.11) is a field equation, a variation of the magnitude of the source term by a factor of three means an change in the thermoacoustically generated power by a factor of nine. The thermoacoustic conversion efficiency is therefore almost an order of magnitude larger than that predicted by the previous theory.

3.3.2 Solution of the Thermoacoustic Wave Equation

In order to obtain a solution to the one dimensional field equation, it is most convenient to transform the equation from the displacement variable to acoustic stress. The reason for transforming is the following. The total strain in a body created by a non-uniform temperature is the sum of the thermally generated strain and the acoustic strain. The acoustic stress, however, is determined only by the acoustic strain [3.2]. Therefore, obtaining an equation in the acoustic stress makes possible the separation of the thermal and acoustic elements of the problem. This is particularly important when using a Green's function approach. The acoustic Green's function represents the propagating element of a given acoustic variable. If the equation is in the displacement or strain variable, these quantities include both a thermal and acoustic contribution. The thermal element does not propagate. Therefore, the acoustic Green's function cannot be used to describe that portion of the variable. If an equation is obtained in acoustic stress, the thermal and acoustic contributions are separated and application of the Green's function approach is very straight forward. Another reason for transforming the equation to the stress variable is that acoustic boundaries can be easily handled, since the thermal distribution does not modify the acoustic boundary condition for stress.

The one dimensional thermoacoustic wave equation (3.11) will now be transformed to an equation in the stress variable, using equation (3.14) derived in the previous section.

$$T_3 = (\lambda + 2\mu)S_3 - 3B\alpha_s\theta \quad (3.16)$$

In another form, this relation becomes

$$S_3 = \frac{T_3}{c_{11}} + \frac{3B\alpha_s\theta}{c_{11}}. \quad (3.17)$$

Since the thermoacoustic wave equation derived earlier was in the variable u_z , the total displacement in the z direction, we can take the derivative of that equation with respect to z , and obtain an equation in the variable S_3 .

$$\frac{\partial^2 S_3}{\partial z^2} + k_a^2 S_3 = \frac{3B\alpha_s}{c_{11}} \frac{\partial^2 \theta}{\partial z^2} \quad (3.18)$$

Substituting the relation found in equation (3.17) into this equation, the thermoacoustic equation in the stress variable is obtained.

$$\frac{\partial^2}{\partial z^2} \left(\frac{T_3}{c_{11}} + \frac{3B\alpha_s \theta}{c_{11}} \right) + k_a^2 \left(\frac{T_3}{c_{11}} + \frac{3B\alpha_s \theta}{c_{11}} \right) = \frac{3B\alpha_s}{c_{11}} \frac{\partial^2 \theta}{\partial z^2} \quad (3.19)$$

There are two identical terms on each side of the equation which cancel, leaving the following.

$$\frac{\partial^2 T_3}{\partial z^2} + k_a^2 T_3 = -3k_a^2 B\alpha_s \theta \quad (3.20)$$

This is the one dimensional thermoacoustic wave equation in the stress variable.

The Green's function for the equation above

$$\frac{\partial^2 G}{\partial z^2} + k_a^2 G = \delta(z - z_0), \quad (3.21)$$

is given by

$$G(z, z_0) = \frac{1}{2jk_a} e^{jk_a |z - z_0|}. \quad (3.22)$$

The solution to the wave equation (3.20) is given by the integral of the product of Green's function G and the source function $-3k_a^2 B\alpha_s \theta$ over the source coordinate z_0 .

$$T_3(z) = \int_{-\infty}^{\infty} -3k_a^2 B\alpha_s \theta(z_0) \frac{1}{2jk_a} e^{jk_a |z - z_0|} dz_0 \quad (3.23)$$

When z is chosen to be far from the thermal source, the equation becomes

$$T_3(z) = \frac{-3B\alpha_s k_a}{2j} e^{-jk_a z} \int_{-\infty}^{\infty} \theta(z_0) e^{jk_a z_0} dz_0 \quad (3.24)$$

This equation indicates that the far field stress amplitude is proportional to the Fourier transform of the temperature distribution, evaluated at the acoustic k -vector k_a .

$$T_3(z) = \frac{-3B\alpha_s k_a}{2j} e^{-jk_a z} \mathcal{F}\{\theta(z)\}|_{k_a}, \quad (3.25)$$

where

$$\mathcal{F}\{\}\big|_{k_a} = \int_{-\infty}^{\infty} \{\} e^{jk_a z_0} dz_0. \quad (3.26)$$

This is the far field stress generated by a one dimensional harmonic thermal distribution in an infinite isotropic elastic medium.

3.3.3 Thermoacoustic Generation near an Acoustic Boundary

To include the effects of an acoustic boundary near the thermal source distribution, the method of images may be used. Adding a mirror image of the thermoacoustic source across the acoustic boundary, with the magnitude and phase of the acoustic reflection coefficient at the boundary, provides an effective thermal source without the boundary which is equivalent to the original distribution with the acoustic boundary. This is shown in Figure 3-1.

$$\theta_{eff} = \theta(z) + r\theta(-z) \quad (3.27)$$

The acoustic reflection coefficient r is determined by the acoustic impedance mismatch at the acoustic boundary.

$$r = \frac{Z_1 - Z_2}{Z_1 + Z_2} \quad (3.28)$$

Z_i is the acoustic impedance of medium i .

If this result is substituted into equation (3.25), the far field stress is given by

$$T_3(z) = \frac{-3B\alpha_s k_a}{2j} e^{-jk_a z} \mathcal{F}\{(\theta(z_0) + r\theta(-z_0))\}|_{k_a}, \quad (3.25)$$

It is a property of Fourier transforms that if

$$\mathcal{F}\{\theta(z)\} = \Theta(k), \quad (3.30)$$

then

$$\mathcal{F}\{\theta(-z)\} = \Theta(-k) \quad (3.31)$$

Therefore, the far field stress generated by a thermal source $\theta(z_0)$ near an acoustic boundary with reflection coefficient r is given by

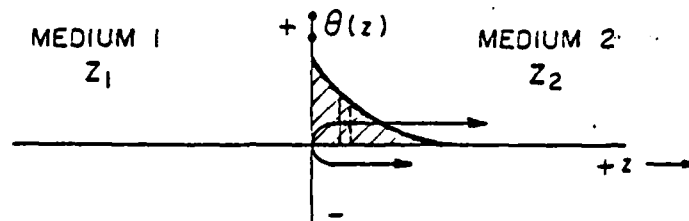
$$T_3(z) = \frac{-3k_a B\alpha_s}{2j} e^{-jk_a z} [\Theta(k_a) + r\Theta(-k_a)], \quad (3.32)$$

where

$$\Theta(k_a) = \mathcal{F}\{\theta(z)\}|_{k_a}. \quad (3.33)$$

THERMOACOUSTIC SOURCES NEAR AN ACOUSTIC BOUNDARY

ACTUAL SOURCE



EFFECTIVE SOURCES IN MEDIUM 2 FOR $+z$ GENERATION

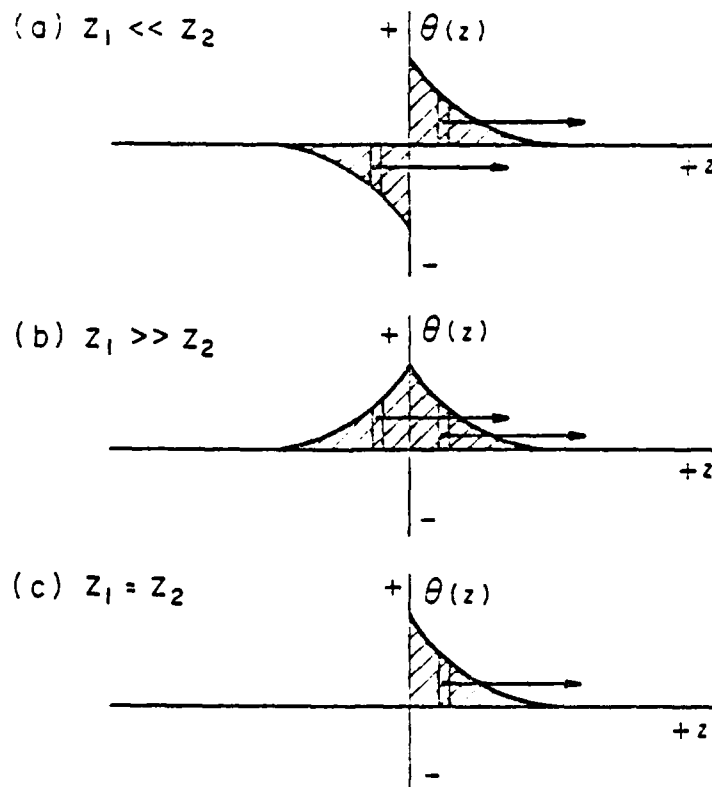


Figure 3-1. Effective thermoacoustic sources near an acoustic boundary.

The formalism above makes possible the simple calculation of all the intermediate cases between the constrained and free surface boundary conditions. To illustrate the effect of the acoustic boundary conditions and frequency of modulation on the thermoacoustic conversion efficiency, the following case will be examined. Two semi-infinite solids of different acoustic impedance are bonded together. One of the solids is transparent and thermally non-conducting. Harmonically modulated light is transmitted through the transparent solid to the interface where it is absorbed in an infinitesimally thin boundary layer of the absorbing solid. The thermal distribution created by the harmonic heating couples to an acoustic wave which propagates away from the interface. The photoacoustically generated power is measured in the optically absorbing solid far from the thermal source. While keeping all other parameters constant, the conversion efficiency is measured as a function of the modulation frequency and the acoustic impedance mismatch. Figure 3-2 contains a family of curves of the conversion efficiency versus modulation frequency for several values of the acoustic reflection coefficient. The reflection coefficient is related to the impedance mismatch at the acoustic boundary by equation (3.28).

There are several interesting features of these curves. At a free surface, the conversion efficiency is proportional to frequency. If a photoacoustic experiment is done in air, the acoustic reflection coefficient r is -.99998. Under this condition, there is strong reason for working at high frequencies. Electron-acoustic imaging is done under vacuum and again the far field thermoacoustic conversion efficiency should increase linearly with frequency.

These results are based upon a one dimensional model. In the final section of this chapter, the three dimension theory will be presented to account for the highly localized nature of the thermal distribution which is most common in practice.

3.4 Thermoacoustic Generation under Spherical Symmetry

In this section, the solution to the thermoacoustic field equation for a point source of harmonically varying power will be presented. The solution of three

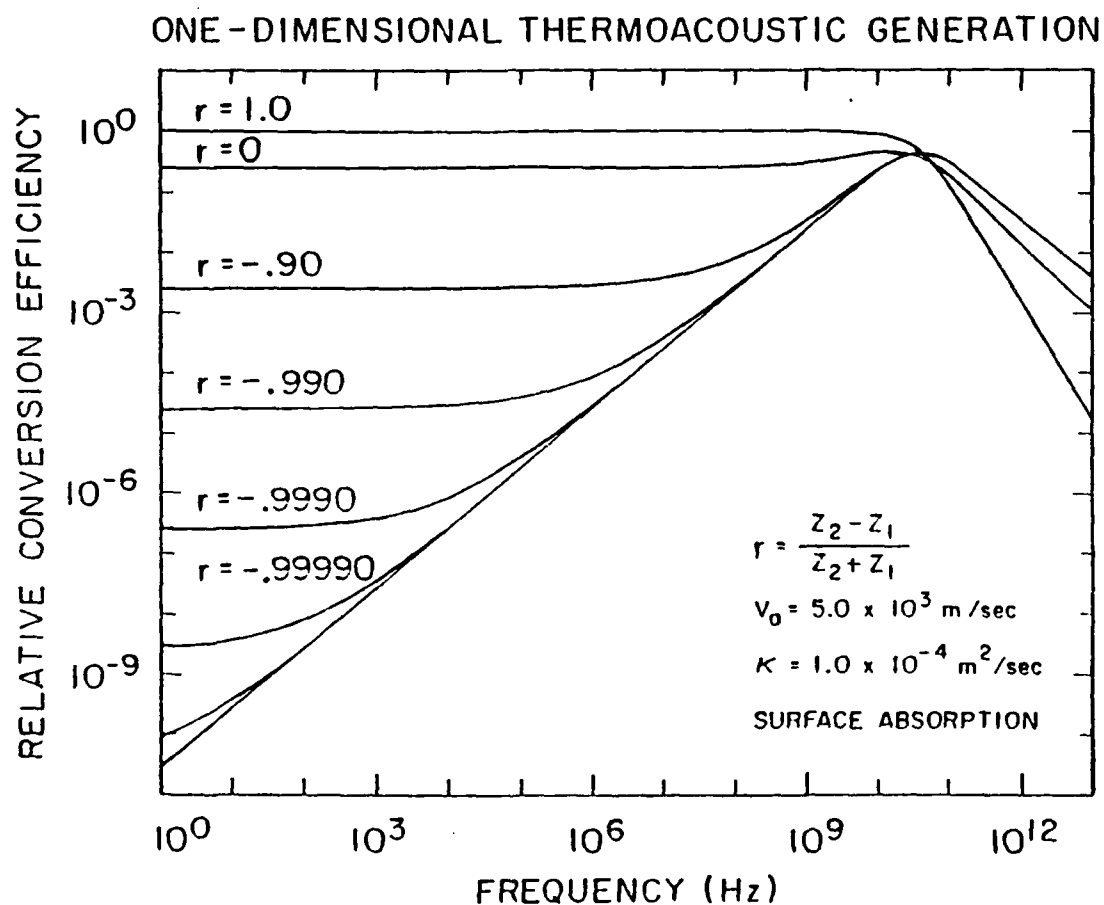


Figure 3-2. The relative photoacoustic conversion efficiency as a function of modulation frequency and acoustic boundary conditions for one dimensional generation of sound.

dimensional problems in solids in general is rather intractable. This case was chosen because it could be solved in a straight forward manner. The results are general, however, in the sense that when the thermal source is small compared to an acoustic wavelength, the actual shape of the source becomes unimportant. The results show that the conversion efficiency increases strongly with frequency.

3.4.1 Thermoacoustic Equation in Spherical Coordinates

The thermoacoustic field equation for an infinite isotropic solid with a non-uniform temperature distribution was derived in section 3.2. The result is shown below.

$$(\lambda + 2\mu)\nabla^2 \bar{u} = \rho \frac{\partial^2 \bar{u}}{\partial t^2} + 3B\alpha_s \nabla \theta. \quad (3.34)$$

To obtain the solution to this equation for a temperature source which is spherically symmetric, a transformation to spherical coordinates is necessary. The symmetry requires that all displacements must be radial, and all derivatives transverse to the radius vector must vanish. In spherical coordinates, equation (3.34) becomes the scalar expression shown below.

$$(\lambda + 2\mu) \frac{\partial}{\partial r} \left(\frac{1}{r^2} \frac{\partial}{\partial r} (r^2 u_r) \right) = \rho \frac{\partial^2}{\partial t^2} u_r + 3B\alpha_s \frac{\partial \theta}{\partial r} \quad (3.35)$$

Integrating with respect to r and differentiating with respect to time, the equation becomes

$$(\lambda + 2\mu) \left(\frac{1}{r^2} \frac{\partial}{\partial r} (r^2 v_r) \right) = \rho \frac{\partial^2}{\partial t^2} \int v_r dr + 3B\alpha_s \frac{\partial \theta}{\partial t}. \quad (3.36)$$

If a velocity potential is defined such that

$$v_r = \frac{\partial \Phi}{\partial r}, \quad (3.37)$$

or equivalently,

$$\Phi = \int v_r dr + \text{constant}, \quad (3.38)$$

equation (3.36) becomes

$$(\lambda + 2\mu)\nabla^2 \Phi = \rho \frac{\partial^2}{\partial t^2} \Phi + 3B\alpha_s \frac{\partial \theta}{\partial t} + \text{constant}. \quad (3.39)$$

The constant is indistinguishable from a uniform temperature change of the entire volume, which will not effect a harmonic excitation and solution. Therefore, the constant can be set to zero, leaving

$$\nabla^2 \Phi - \left(\frac{1}{V_a^2} \right) \frac{\partial^2 \Phi}{\partial t^2} + \left(\frac{3B\alpha_s}{\lambda + 2\mu} \right) \frac{\partial \theta}{\partial t}, \quad (3.40)$$

where $V_a^2 = (\lambda + 2\mu)/\rho$ and $v_r = \partial \Phi / \partial r$. This is the thermoacoustic field equation for a spherically symmetric thermal source in an infinite isotropic elastic medium. In the next section, the temperature distribution generated by a harmonic point source of heat will be calculated for substitution into this equation.

3.4.2 Temperature Distribution for a Periodic Point Source

The solution for a harmonically varying point source of heat in an infinite isotropic solid has been derived [3.8]. For a harmonic source of power released from a point at the origin of an infinite isotropic medium,

$$P_0 \delta^3(r) e^{j\omega t}, \quad (3.41)$$

the steady state temperature distribution is

$$\theta(r, \omega) = \frac{P_0}{4\pi K} \left(\frac{e^{-k_t r}}{r} \right) e^{j\omega t}. \quad (3.42)$$

3.4.3 Spherical Solution

Substitution of equation (3.42) into the acoustic field equation (3.40) results in the following expression,

$$\nabla^2 \Phi + k_a^2 \Phi = \gamma \frac{e^{-j k_t r}}{r}, \quad (3.43)$$

where

$$\gamma = \left(\frac{3B\alpha_s}{\lambda + 2\mu} \right) \left(\frac{j\omega P_0}{4\pi K} \right). \quad (3.44)$$

The general solution to this equation is given by

$$\Phi = \frac{ae^{-jk_a r}}{r} + \left(\frac{\gamma}{k_t^2 + k_a^2} \right) \frac{e^{-k_t r}}{r}. \quad (3.45)$$

To determine the coefficient a , a boundary condition must be used. By symmetry, the radial velocity must be zero at the origin. This means that the gradient of the potential function must be zero at the origin. Under these conditions, the total solution is

$$\Phi = \frac{-\gamma}{k_t^2 + k_a^2} \left(\frac{e^{-jk_a r}}{r} - \frac{e^{-k_t r}}{r} \right). \quad (3.46)$$

To examine the efficiency of photoacoustic conversion, a calculation of the far field acoustic power radiated from the source can be made. Since the total far field power radiated is independent of the distance from the source, the calculation can be done at a distance where the plane wave impedance can be used. Under this condition, the radial velocity is given by

$$v_r \approx \left(\frac{jk_a \gamma}{k_t^2 + k_a^2} \right) \left(\frac{e^{-jk_a r}}{r} \right). \quad (3.47)$$

The plane wave impedance is

$$Z_0 = \frac{-T_r}{v_r} = -\rho V_a. \quad (3.48)$$

Integrating the power density over a spherical surface far from the origin, the total power radiated is

$$P = 2\pi(\rho V_a) \left(\frac{3B\alpha_s}{\lambda + 2\mu} \right)^2 \left(\frac{P_0}{4\pi K} \right)^2 \frac{\omega^2 k_a^2}{|k_t|^4 + k_a^4}. \quad (3.49)$$

In another form,

$$P = 2\pi(\rho V_a) \left(\frac{3B\alpha_s}{\lambda + 2\mu} \right)^2 \left(\frac{P_0}{4\pi K} \right)^2 \frac{\kappa^2 k_a^2}{\left(1 + \frac{\omega^2 \kappa^2}{V_a^4} \right)}. \quad (3.50)$$

This is an expression for the total far field acoustic power generated by a harmonic point source of heat.

3.4.4 Frequency Dependence of Thermoacoustic Coupling

We now consider the frequency dependence of the photoacoustic conversion efficiency. In most solids, at frequencies below 10 GHz,

$$\frac{\omega^2 \kappa^2}{V_a^4} \ll 1. \quad (3.51)$$

Under this condition, equation (3.50) becomes

$$P = 2\pi \left(\frac{\rho}{V_a} \right) \left(\frac{3B\alpha_s}{\lambda + 2\mu} \right)^2 \left(\frac{P_0}{4\pi} \right)^2 \left(\frac{1}{\rho C} \right)^2 \omega^2. \quad (3.52)$$

Note that the radiated power is proportional to the square of the modulation frequency. Thus the conversion efficiency increases very fast with modulation frequency for highly localized heat sources.

Equation (3.52) does not include the effects of an acoustic boundary on the conversion efficiency. When the source is near an acoustic boundary, the theory of one dimensional generation can be used to understand the frequency dependence of the conversion efficiency. The one dimensional theory showed that a free surface increases the frequency dependence of the conversion efficiency. This is due to the fact that the reflections from the free surface tend to cancel the forward propagating waves. At low frequencies, they cancel almost exactly. At higher frequencies, the cancellation is less. Thus, the overall coupling increases with frequency in the presence of the free surface. This means that the thermoacoustically generated power radiated to the far field goes as

$$P \propto \omega^N \quad (3.53)$$

where $N > 2$ when the three dimensional thermal source is near a free surface.

It is clear that when the thermal source size is small compared to the acoustic wavelength, the modulation frequency should be as high as is possible for optimal conversion efficiency. One dimensional theory does not predict this in the constrained case, and predicts only an increase proportional to the frequency in the free surface case. This strong dependence of the conversion efficiency on frequency is one reason for photoacoustic imaging at high frequencies. When imaging with high resolution, the thermal spot size will always be small compared to an acoustic wavelength. These results are therefore very applicable for calculating the conversion efficiencies.

References for Chapter 3

- [3.1] R. M. White, "Generation of Elastic Waves by Transient Surface Heating," *J. Appl. Phys.* **34**, 3559 (1963).
- [3.2] A.E. Love, *The Mathematical Theory of Elasticity*, Cambridge: Cambridge University Press, 1927 (Dover reprint, 1944), 4th ed., p. 108.
- [3.3] B.A. Auld, *Acoustic Fields and Waves in Solids*, Vol. 1, New York: John Wiley and Sons, 1973, p. 27.
- [3.4] I.S. Sokolnikoff, *Mathematical Theory of Elasticity*, Florida: Robert E. Krieger Publishing Company, 1983, p. 359.
- [3.5] R.C. Bray, *Acoustic and Photoacoustic Microscopy*, Ph.D. Thesis, Stanford University, 1981, p. 116.
- [3.6] Allan Rosencwaig, *Photoacoustic and Photoacoustic Spectroscopy*, New York: John Wiley and Sons, 1980, p. 126.
- [3.7] John Opsal and Allan Rosencwaig, "Thermal-wave depth profiling: Theory," *J. Appl. Phys.*, **53**, 4210 (1982).
- [3.8] H.S. Carslaw and J.C. Jaeger, *Conduction of Heat in Solids*, Oxford: Oxford University Press, 1980, p. 263.

Chapter 4.

HIGH RESOLUTION PHOTOACOUSTIC IMAGING

4.1 Introduction

One of the interesting characteristics of photoacoustic imaging is that light can be used to periodically deposit heat over a region that is small compared to an acoustic wavelength. Under this condition, the periodic thermal distribution generates a spherically diverging sound wave. Efficient detection of the acoustic power in this spherical wave is not possible with phase sensitive planar acoustic transducers. The reason for the inefficiency is the requirement that the phase of the wave vary no more than one half wavelength over the aperture of the transducer. If the transducer is placed near the source, much of the power falls within the transducer aperture, but the spacial phase variation over the aperture greatly reduces the efficiency of transduction. If the transducer is placed far from the source distribution, the phase of the incident acoustic field is uniform across the aperture, but little of the total power is collected. The solution to the problem of efficiently detecting the diverging power is to collimate it with an acoustic lens. This collimation can improve the sensitivity of the detection system by orders of magnitude.

The concept of using an acoustic lens to collimate and detect photoacoustically generated sound was first demonstrated in 1978 by Wickramasinghe et al. [4.1]. An acoustic lens was used to collect sound generated by a highly focused optical beam. The sample was scanned relative to the fixed optical and acoustic lenses to obtain a photoacoustic image. The system used for this initial demonstration was not optimal, however. The laser used to generate the sound was not modulated efficiently, generating sound over a frequency range of more than 5 GHz. The acoustic lens used was larger than necessary, requiring that the sound propagate

through a relatively long water path. The acoustic loss in the water was reported to be 32 db. Because the system was pulsed, the detection bandwidth required was approximately 10 MHz. As a result of the inefficiency of the generation and detection system, very high peak temperatures were required to obtain reasonable signals. The images indicated that the required temperatures were near the melting point of the materials imaged. Bray [4.2] continued this work and indicated that even after improvements to the system, temperatures of several hundred degrees were required to obtain only modest signal to noise ratios. Since these initial efforts, several improvements have been included in a newly built system. These improvements have increased the sensitivity of this technique by orders of magnitude, requiring only small peak temperatures and optical peak powers.

In this chapter, two photoacoustic experiments will be described which make use of an acoustic lens for the collimation and detection of high frequency photoacoustically generated sound. In the first experiment, an acoustic lens is used to collect photoacoustic sound generated in thin films on optically transparent substrates. In the second experiment, the use of gallium as a coupling liquid has made possible the detection of sound generated in optically opaque materials. These experiments will be described, and images will be presented demonstrating the sensitivity and resolution of these techniques.

4.2 Experimental Description

The experimental arrangement is shown in Figure 4-1. A modulated laser beam is focused by an optical microscope objective through the transparent sample substrate to a small spot on the film to be imaged. An acoustic lens is positioned to be confocal with the optical lens. The modulated optical power photoacoustically generates sound in the region of the optical spot. Because the optical spot size is generally smaller than an acoustic wavelength, the sound diverges from the source as a spherical wave. This sound propagates from the heated surface to the acoustic lens through a coupling liquid, where it is collimated. The collimated sound then

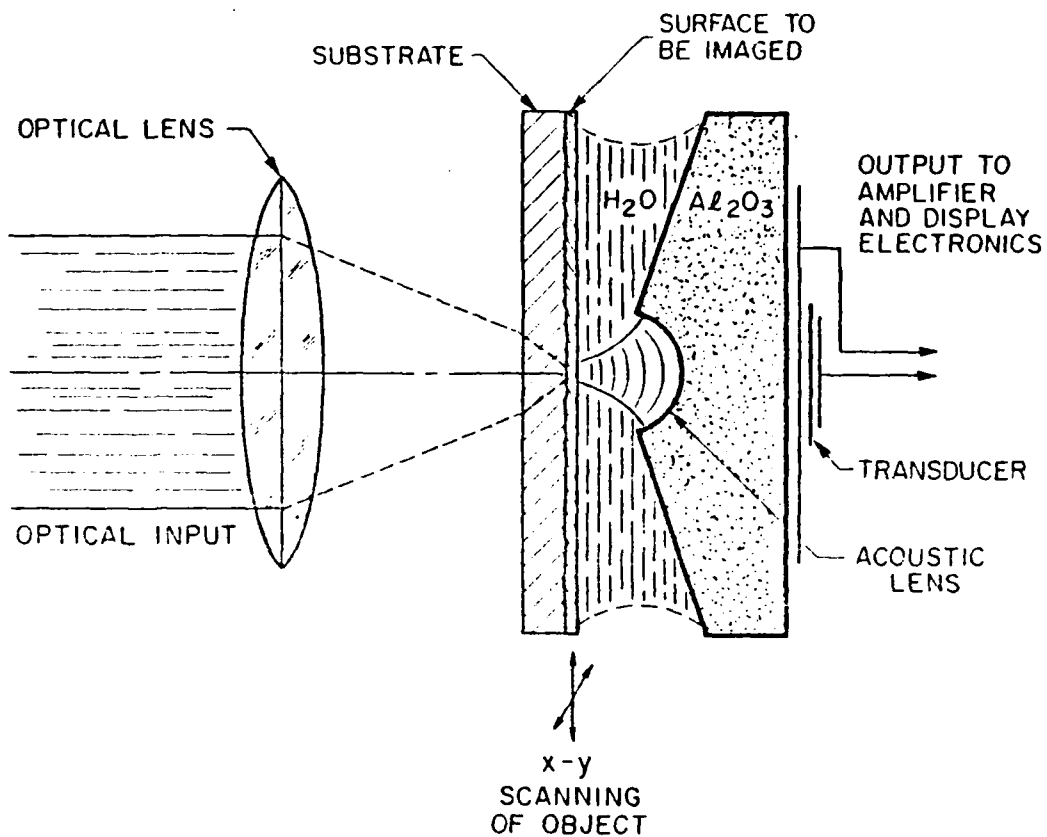


Figure 4-1. The experimental arrangement for photoacoustic imaging of thin films on optically transparent substrates using an acoustic lens to collect the sound generated by the modulated optical power.

propagates to a thin film zinc-oxide piezoelectric transducer, where an RF signal is generated. The RF signal is sent to a low noise preamplifier, after which it is further amplified, filtered and finally detected with a crystal detector.

The sample is scanned with respect to the fixed acoustic and optical lenses to generate an image which maps the photoacoustic conversion efficiency as a function of position on the sample. The scanning is done at 30 Hz in one dimension, and slow scanned in the other dimension. The X and Y position of the sample is detected using linear variable differential transformers. The two dimensional position and the photoacoustic signal are sent to a scan converter which displays the photoacoustic signal as a function of position on a high resolution television screen. An image can be obtained in 15 seconds if a 30 kHz detection bandwidth is chosen.

The alignment of the acoustic lens with respect to the optical spot is very tedious, requiring a two dimensional search for a small signal which emanates from the film over an area of approximately one square micron. To eliminate one of the degrees of freedom in the search, a electromechanical scanner was also built to scan the lens with respect to a fixed sample and optical spot. By scanning the acoustic lens in one dimension at 30 Hz, the photoacoustic response over a line is obtained. This photoacoustic line response can be displayed on a CRT screen in real time. By slowly translating the lens in the direction perpendicular to the fast scan, a one dimensional search for the photoacoustic spot can be made.

Modulation of optical power at frequencies near 1 GHz is not a trivial task. Fortunately, external modulation was made unnecessary by the use of a cavity dumped argon laser. The cavity dumped argon laser consists of a fused quartz Bragg cell placed in the folded cavity of a Spectra-Physics Model 166 Argon ion laser. The arrangement is such that light can be diffracted out of the laser cavity by 470 MHz sound which traverses the Bragg cell. There are two diffracted components which leave the laser cavity, one which is upshifted by 470 MHz, the other down shifted by the same frequency. Because these two components are spatially superimposed, they beat against each other to produce a power or intensity modulation at twice

this frequency, or 940 MHz. This argon laser is capable of delivering 20 nanosecond optical pulses at a rate of up to 1 MHz with peak powers near 50 watts.

A second source of modulated optical power used was a gallium aluminum arsenide diode laser [4.3]. It supplies up to 5 mW of optical power in a single transverse and single axial mode. A circuit was built to allow direct current modulation of the device at frequencies near 1 GHz. The modulation efficiency was measured on a sampling scope. See Figure 4-2. Taking into account the roll off of the PIN photodiode [4.4] used to detect the optical modulation, the modulation depth is estimated to be near 100 percent.

4.3 Sensitivity of the Acoustic Lens as a Photoacoustic Detector

Since the photoacoustic conversion efficiencies are rather small, the sensitivity of the acoustic lens makes it attractive for collecting photoacoustically generated

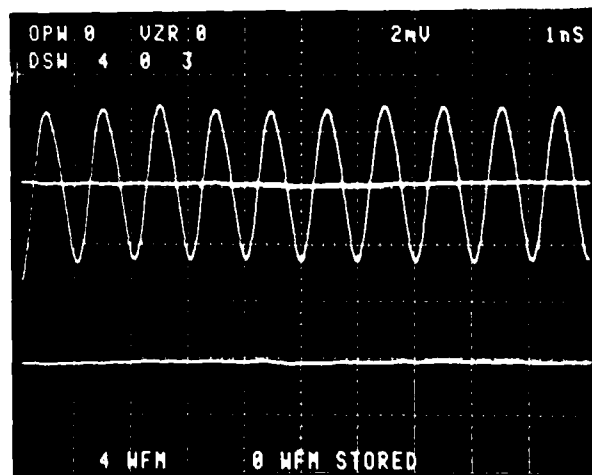


Figure 4-2. The modulation depth of the output of an NEC NDL3000 diode laser at a frequency of 1 GHz.

power Using the three dimensional theory presented in Chapter 3, a calculation can be made of the expected signal to noise ratio under typical photoacoustic imaging conditions. This calculation is shown in Table 4-1 below.

TABLE 4-1

Photoacoustic Sensitivity with an Acoustic Lens

Optical power focused to $1 \mu^2$ area	10^{-3} Watts
Photoacoustic conversion efficiency	10^{-9}
Generated acoustic power	10^{-12} Watts
Acoustic collection efficiency	10^{-2}
Detected power	10^{-14} Watts
Johnson noise power (10^4 Hz bandwidth)	10^{-16} Watts
Signal to Noise ratio	100

To experimentally verify the predicted sensitivity, a current modulated diode laser [4.3] was focused to approximately one square micron onto the surface of a 1000 Å thick gold film pattern on a glass substrate. The object was then scanned across the pattern, generating the a-trace seen in Figure 4-3. Approximately 0.5 mW of the optical power was absorbed by the gold film. The bandwidth of the detection system was 10 kHz. The experimentally measured sensitivity is near that calculated in Table 4-1.

4.4 Photoacoustic Imaging Results

In this section, the images obtained with the photoacoustic imaging system described in the previous sections will be presented and discussed. The images presented include recrystallized silicon and gold films on transparent substrates.

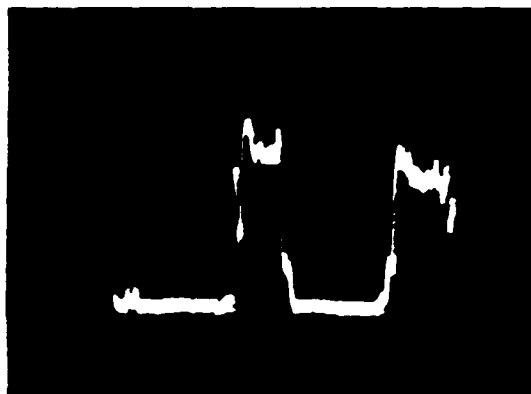


Figure 4-3. The signal to noise ratio obtained using less than 1 mW of optically absorbed power to generate sound in a 1000 Å thick gold film on a glass substrate.

4.4.1 Laser Recrystallized Silicon Film on a Quartz Substrate

Some interest has been shown in laser annealing and recrystallization of thin films deposited upon various substrates [4.5,4.6]. Laser recrystallization of solids is inherently traumatic, requiring rapid temperature changes and large spacial gradients of temperature. Furthermore, the melting and subsequent recrystallization of thin films takes place next to a substrate whose lattice constant, expansion coefficient and stiffness are generally different than those of the film. These conditions generally leave the recrystallized film cracked and under stress.

Since the photoacoustic conversion efficiency is integrally tied to the mechanical and thermal properties of a material, it was thought that photoacoustic imaging of these films might provide some information about the recrystallization process. With this in mind, a recrystallized silicon sample was obtained from the research group

of Prof. J.F. Gibbons group at Stanford University [4.7]. Using an cw argon ion laser with some beam shaping, a 0.5 micron polysilicon film on a quartz substrate with 500 Å grain size was recrystallized to produce grains with dimensions up to 100 microns. Simultaneously, large thermally induced cracks in the recrystallized film were also produced. These can be clearly seen in the acoustic and photoacoustic images in Figure 4-4 on the following page. Another region of the recrystallized film is shown in Figure 4-5 with optical (DIC) and acoustic comparisons.

Within these obvious cracks, faint evidence of the grain and subgrain boundaries can be seen in the acoustic images. The contrast from grain to grain is very small, however. In the photoacoustic images, there is a strong contrast between the grains. A measurement of the photoacoustic contrast indicated that the variation in photoacoustic power from grain center to grain center was as large as 8 db. This is shown by the photoacoustic a-trace in Figure 4-6.

It is apparent from the images in figures 4-4 and 4-5 that both the optical (DIC) and the acoustic images contain much more information about the topography of the sample than does the photoacoustic image. The strong dependence upon topography makes it difficult to extract materials information from these optical and acoustic images.

The large change in the photoacoustic conversion efficiency from grain to grain was somewhat puzzling. Using a one dimensional numerical routine for modeling the photoacoustic generation [4.8], the far field photoacoustic power was calculated while varying the material parameters of the silicon. The results indicated there was no reasonable variation of the material properties that could explain the large contrast seen in these images. The calculations showed that the photoacoustic power generated was almost independent of the thermal conductivity, and acoustic stiffness. There was a strong dependence upon the expansion coefficient and specific heat, but it was argued that these material properties could not vary by factors of two from grain to grain. The optical absorption was eliminated as a possible source of contrast by imaging the sample in optical transmission both under very strong



FIELD SIZE 300 μm

ACOUSTIC REFLECTION (1GHz)



PHOTOACOUSTIC (1GHz)

RECRYSTALLIZED SILICON FILM (0.5 μm) ON QUARTZ SUBSTRATE

Figure 4-4. Acoustic and photoacoustic images of an area of laser recrystallized silicon film on a quartz substrate.



ACOUSTIC
REFLECTION (1GHz)



PHOTOACOUSTIC
(1GHz)



OPTICAL

FIELD SIZE 200 μm

LASER RECRYSTALLIZED SILICON (0.5 μm) ON QUARTZ SUBSTRATE

Figure 4-5. A comparison of acoustic, photoacoustic and optical (DIC) images of the laser recrystallized silicon sample.

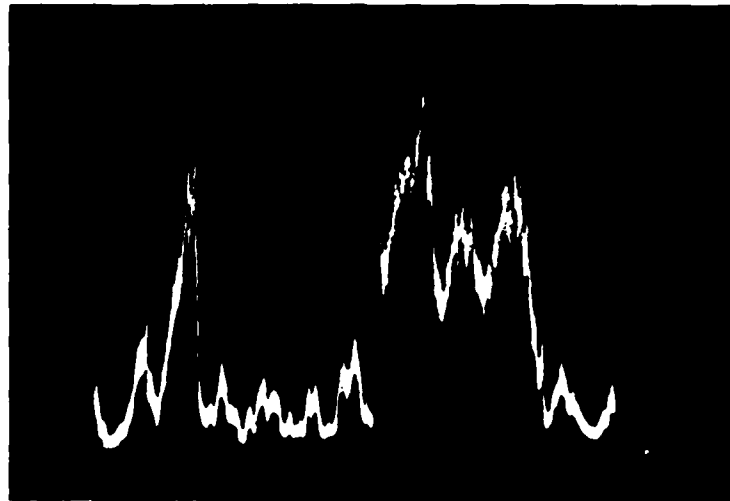


Figure 4-6. An a-trace illustrating the variation of the photoacoustic signal from grain to grain in the recrystallized silicon sample.

and weak illumination. These optical images showed no contrast between the grains which had shown large photoacoustic variations.

A suggestion was made [4.9] that the source of contrast could be the orientation of the grains. Because the generation efficiency is dependent upon the bulk modulus of the material, it seemed possible that the anisotropy of the silicon could make the conversion efficiency dependent upon the crystalline orientation. A calculation was therefore made of the effective bulk modulus of silicon as its stiffness tensor is rotated. This modulus was then used in the numerical calculation of the conversion efficiency. The result was that the predicted far field photoacoustic power did depend upon the orientation of the grains. However, the largest predicted variation in the signal due to orientation was 1.3 db, much smaller than the measured variation. Another confirmation that the source of the contrast was not grain orientation was some diffractometer analysis. The analysis indicated that much less

than one percent of the grains had orientations different from $\langle 100 \rangle$ normal to the surface. The contrast seen in the photoacoustic images was very wide spread, involving greater than 20 percent of the sample area. Therefore, orientation is ruled out as the source of contrast.

An alternative source of contrast is the adhesion of the grains to the substrate. If the grains are not uniformly bonded to the substrate, the photoacoustic conversion efficiency will vary from point to point. This possibility was also numerically modeled. The results indicated that the expected variation of the conversion efficiency from a well adhered grain to a grain that was completely free was 5.5 db. This is the most plausible explanation of the contrast seen in the photoacoustic images.

Confirmation of this conclusion came in two ways. First, the acoustic reflection images showed high reflectivity in the regions where the photoacoustic conversion efficiency was low. This is consistent with the adhesion model because when a grain is poorly adhered to the substrate, the acoustic reflectivity in that region should be unity. The acoustic contrast between well and poorly bonded grains was small, however. This is due to the fact that the impedance mismatch between water and the silicon is very large. Even when a grain is well adhered to the substrate, there is a very large acoustic reflection at the silicon/water interface. Second, application of scotch tape to the sample surface did remove some of the dark grains after repeated attempts. The grains were difficult to remove however. This could be attributed to the very sharp boundaries that existed between grains. Under these conditions, it is conceivable that even with no bonding to the substrate, the grains could still be difficult to extract from their locations. These results led to the conclusion that the source of contrast in the images is due to the adhesion properties of the individual grains.

4.4.2 Thin Gold Film on a Glass Substrate

A patterned 1000 Å gold film on a glass substrate was imaged using the photoacoustic imaging system described in section 4.2. The results are shown in

Figure 4-7. The optical image (c) indicates that there are small bubbles or defects below the film in certain areas. In the photoacoustic image (a), it is very apparent that in these regions the photoacoustic conversion efficiency is very much reduced relative to the average photoacoustic response. As was shown in the previous section, the photoacoustic conversion efficiency is strongly dependent upon the adhesion of films to the substrate. This is the source of contrast in the photoacoustic image. Only a slight contrast is seen in the acoustic image. This is due to the fact the the acoustic lens is focused onto the surface of the film. At this focal position, the acoustic sensitivity to adhesion is rather poor.

The photoacoustic technique is inherently more sensitive to the adhesive properties of thin films than acoustic reflection for the following reason. If the thickness of a film is very small compared to an acoustic wavelength, it only slightly perturbs the acoustic impedance and velocity of the substrate. Since the mismatch in impedance between water and most solids is very large, the reflection from the substrate is almost independent of the properties of the film. This large background reflectivity limits the sensitivity of acoustic reflection techniques when examining thin films on substrates. In contrast, the photoacoustic signal does not contain a large background signal. The boundary condition under which sound is photoacoustically generated can affect the conversion efficiency by orders of magnitude as was shown in section 3.3.3. This makes it an attractive technique for examination of thin films with adhesion problems.

4.5 Photoacoustic Imaging of a Free Surface

One limitation of the technique just described is the requirement that the sample must have a transparent substrate. The reason for this is that the imaging is done in transmission. The optical power is focused from one side and the acoustic lens collects the sound from the other. Since the velocity and impedance mismatch between water and most solids is very large, the acoustic lens must be focused directly onto the surface to be imaged while the optical beam is focused to the same surface through the substrate.



(a) PHOTOACOUSTIC



(b) ACOUSTIC (IN FOCUS)



(c) OPTICAL

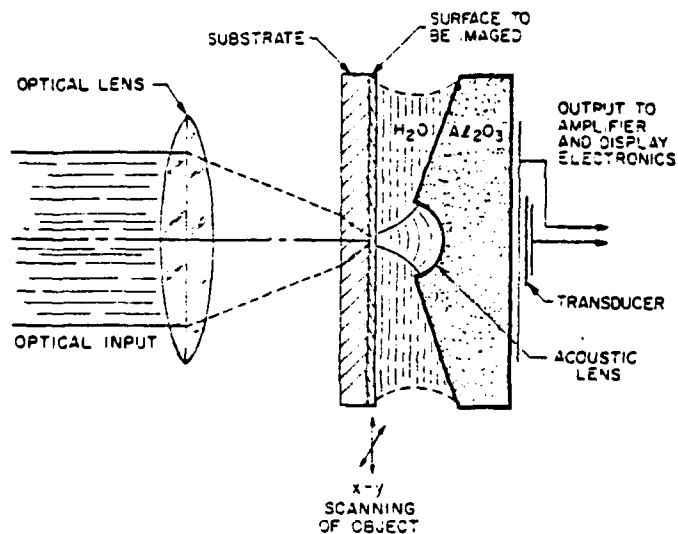
Figure 4-7. A comparison of photoacoustic, acoustic and optical images of a gold film on a glass substrate.

There are many important materials and systems which do not have optically transparent substrates. These materials cannot be evaluated with the previous technique. While these material may be optically opaque, they generally are acoustically transparent well beyond 1 GHz frequencies. It is therefore conceivable to focus the optical power onto the front surface of these materials and collect the sound through the substrate or bulk of the sample. Figure 4-8 contains a comparison of the two configurations. The upper figure is the water coupled system described in section 4.2. In the lower figure, the sample has been reversed to allow the light to be directly focused on to the surface to be imaged. The photoacoustic power is then collected through the sample substrate or bulk.

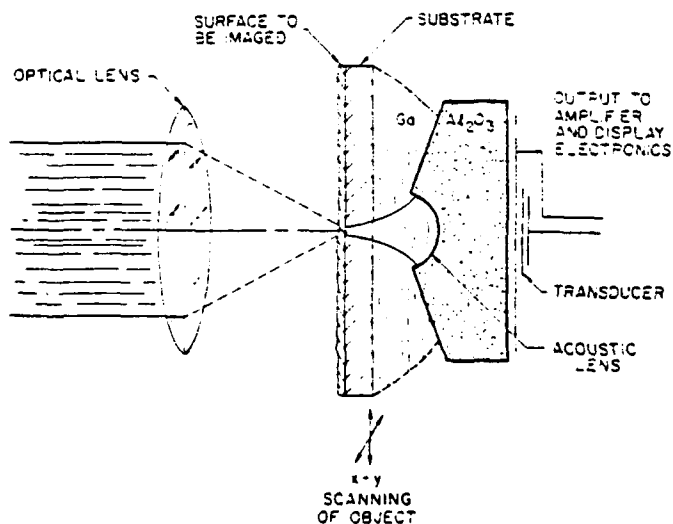
There are several reasons why collecting the sound through the sample substrate is difficult. Since there is a large acoustic impedance mismatch between solids and most liquids, the power transfer across the interface can be very poor. The velocity mismatch between liquids and solids causes considerable aberration in the focused acoustic beam, further reducing the collection efficiency. The strong refraction at the interface also makes it difficult to focus the lens very far into the interior of the solid.

These problems were addressed by Jipson [4.10] in 1979. He demonstrated the use of an acoustic lens in imaging interior planes of a solid using liquid gallium as a coupling liquid. Liquid gallium has three important features. First, it's acoustic impedance is very near that of most solids. Therefore the power transfer across the solid/gallium interface is good. Second, the acoustic velocity of the gallium is approximately two times larger than that of water. This means that the refraction that takes place at the interface between the solid and the gallium is much more tolerable. The third feature is a very low attenuation. This is important because large acoustic lenses are required to image interior planes of a solid, since the backsurface of the object must be brought into focus while the lens remains some finite distance away from the front surface.

The work of Jipson indicated that collection of photoacoustically generated sound through the bulk of the sample could be done. To demonstrate this possibility,



PHOTOACOUSTIC IMAGING OF A LOADED SURFACE



PHOTOACOUSTIC IMAGING OF A FREE SURFACE

Figure 4-8. A comparison of the two ways in which photoacoustically generated sound may be collected by an acoustic lens. In the upper figure, the sound is collected from the surface of the solid with water coupling. In the lower figure, collection takes place through the bulk of the sample with gallium as the acoustic coupler between the sample and the lens.

several large acoustic lenses were made [4.11]. The radius chosen was 250 microns, which allowed imaging through 150 microns of solid with some reasonable working distance. The lenses were tuned to 940 MHz. The same laser, scanning system, and RF detection system were used as with the case of the water coupled system described in section 4.2.

A sample was prepared by depositing a patterned 1000 Å gold film upon a 140 micron glass substrate. The sample was then placed in the photoacoustic imaging system with the film toward the optical lens. The film was first imaged through the substrate in pulsed acoustic reflection mode. This is shown in the left side of Figure 4-9. The photoacoustic image is shown on the right.

The resolution of the acoustic image is poor relative to that seen in the photoacoustic image. There are two reasons for this fact. The first is that since the acoustic velocity of the solid is high, the wavelength of the incident sound is large compared to the optical spot size which essentially determines the resolution in the photoacoustic case. The second is that the refraction that takes place at the solid gallium interface also spreads the acoustic focus. These two effects combine to produce a poorer resolution.

It is worth noting that when imaging in acoustic reflection, the acoustic reflection coefficient as seen from the substrate is near unity whether or not the patterned gold film is present on the substrate. The acoustic contrast, therefore, is largely due to the scattering of the focused sound at the boundaries of the gold film rather than an impedance variation in the sample. For this reason, the contrast seen in the acoustic image of Figure 4-9 is largely found at the edges of the gold film pattern.

The photoacoustic image indicates micron resolution. There is an interesting interference effect in the image. Apparently, the localized thermal excitation couples to a surface wave which propagates to the film boundary where it is partially reflected. It then propagates back to the source region, reradiating some of its energy out into the solid. The reradiated energy interferes with the thermoacoustic

IMAGING THROUGH SUBSTRATE



Acoustic Reflection



Photoacoustic

Field Size 100 micron

Frequency 1 Ghz

1000 Angs. Gold on 140 micron Glass Substrate

Figure 4-9. A comparison of acoustic and photoacoustic images of a gold film, obtained using gallium to collect the sound through the glass substrate of the sample.

source radiation producing a spacially periodic variation of the signal near the boundaries of the patterned gold.

The wetting of the acoustic lens with the liquid gallium was not found to be very difficult if the lens and gallium were kept clean. The fact that the radius of curvature of the lens was relatively large ($250\text{ }\mu\text{m}$) helped minimize the wetting problems. Mercury was also used. The difficulty found in using mercury is that its surface tension is too large. The only way to use it is to obtain a mercury ball somewhat smaller than the hemispherical lens and place it inside. However, with the sample moving rapidly below the ball of mercury, it is difficult to keep the ball inside the acoustic lens for long periods of time. It did seem possible, however, that if a large lens was designed to more completely enclose the mercury, the mercury could be a good coupler from the lens to the sample.

This technique was also used to image the recrystallized silicon sample discussed in section 4.4. In order to achieve proper wetting of the gallium on the silicon, it is very critical that the silicon surface be very clean. The images obtained using this technique also confirmed the non-uniform adhesion of the grains in the laser recrystallized silicon film.

References for Chapter 4

- [4.1] H.K. Wickramasinghe, R.C. Bray, V. Jipson, C.F. Quate, and J.R. Salcedo, *Appl. Phys. Lett.* **33**, 923 (1978).
- [4.2] R.C. Bray, *Acoustic and Photoacoustic Microscopy*, Ph.D. Thesis, Stanford University, 1981, p. 102.
- [4.3] NEC laser diode, Model NDL3000, wavelength 780 nm.
- [4.4] PIN photodiode, Model 5082-4207, Hewlett-Packard, *Optoelectronics Designer's Catalog*, 1983, p. 148.
- [4.5] A. Gat, L. Gerzberg, J.F. Gibbons, "CW laser anneal of polycrystalline silicon: crystalline structure, electrical properties," *Appl. Phys. Lett.* **33**, 775 (1978).
- [4.6] T.J. Stultz and J.F. Gibbons, "The use of beam shaping to achieve large-grain cw laser-recrystallized polysilicon on amorphous substrates," *Appl. Phys. Lett.* **39**, 498 (1981).
- [4.7] T.J. Stultz supplied the laser recrystallized silicon samples.
- [4.8] R.C. Bray, *Acoustic and Photoacoustic Microscopy*, Ph.D. Thesis, Stanford University, 1981, p. 179.
- [4.9] John A. Hildebrand, private communication.
- [4.10] V.B. Jipson, "Acoustic microscopy of interior planes," *Appl. Phys. Lett.* **35**, 385 (1979).
- [4.11] S. Hubbard helped design and prepare the acoustic lenses used in the gallium coupled photoacoustic experiment.

Chapter 5.

HIGH RESOLUTION PHOTOTHERMAL LASER PROBE

5.1 Introduction

At frequencies near 1 GHz, the acoustic wavelength in argon gas becomes half that of visible light, making possible collinear Bragg scattering of laser light by the sound. This acousto-optic interaction has been exploited in a new photothermal laser probe to provide a very high resolution technique for measuring the photothermal response of materials. The probe has several features which are attractive. Since the operating frequency is high, the thermal wavelength in solids is generally small compared to the wavelength of light. Under this condition, the resolution is determined by the optical spot diameter of the probe beam, which can be less than one micron. The probe is an optical technique which does not require either acoustic transducers or contact with the solid being evaluated. Only small optical input powers are necessary to obtain reasonable signal to noise ratios due to its high sensitivity.

The photothermal probe has been implemented in the following arrangement. An intensity modulated pump beam is tightly focused onto the surface of a solid in a cell filled with argon gas at high pressure. See Figure 5-1. The modulated pump beam generates a harmonic temperature distribution which couples to an acoustic wave in the gas at the surface of the solid. A second beam, the probe, is collinearly aligned with the pump and also tightly focused to the same location on the sample. When the modulation frequency of the pump beam is near 1 GHz, the collinear Bragg scattering condition is met and a portion of the probe beam is back scattered or back reflected from the sound propagating in the gas. The light which is scattered from the sound in the gas is upshifted in frequency, so it can be heterodyned in an optical detector with the probe light which is reflected

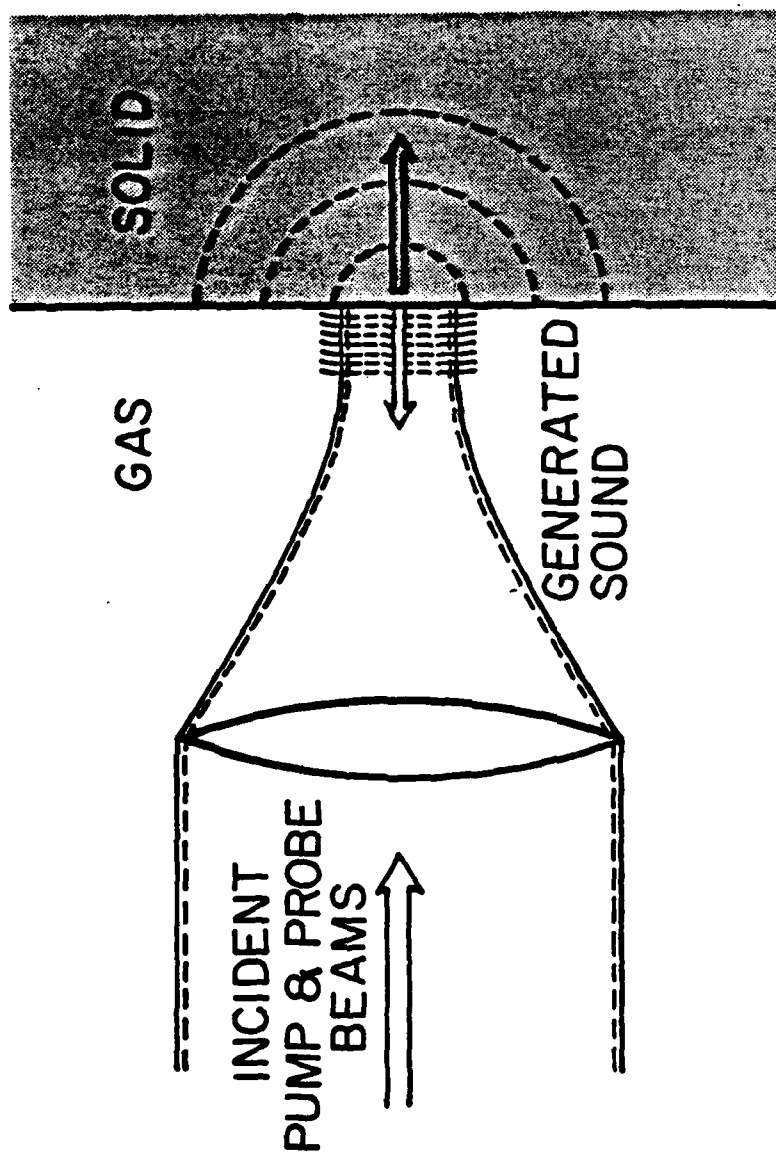


Figure 5-1. The geometry of the photothermal laser probe.

from the solid surface. See Figure 5-2. As will be explained in later sections, the heterodyne signal is proportional to the ac surface temperature over the region of the solid illuminated by the tightly focused probe beam. A photothermal image is obtained by scanning the object in two dimensions relative to the pump and probe beams. This provides a measure of the thermal properties of the solid with high spacial resolution.

In this chapter, the theoretical basis for the photothermal sensitivity of the probe will be presented. The sensitivity will be calculated with argon gas as the coupling medium. A figure of merit will also be established by which various coupling media may be evaluated. A comparison will then be made between three high resolution photothermal and photoacoustic techniques. Finally, an experimental description and verification of the theory will be presented including high resolution photothermal images of boron implanted silicon.

5.2 Derivation of the Bragg Scattering Efficiency

Acoustic Bragg scattering of light is a non-linear interaction. It can be treated formally by calculating the non-linear polarization created when optical and acoustic fields are superimposed. This non-linear optical polarization radiates light at the sum and difference frequency of the two interacting optical and acoustic fields. The total power reradiated at the sum and difference frequency depends upon the summation of the fields over the source region. In this section, it will be shown that the Bragg scattered electric field strength is proportional to an integral of the non-linear source polarization over the interaction region. The strength of the non-linear polarization will then be calculated using the photoelastic relation for the gas. Finally, these results will be combined to provide a relationship between the driving acoustic field in the gas and the scattered electric field strength. From this relation, an effective Bragg reflectivity as seen by the probe beam will be established.

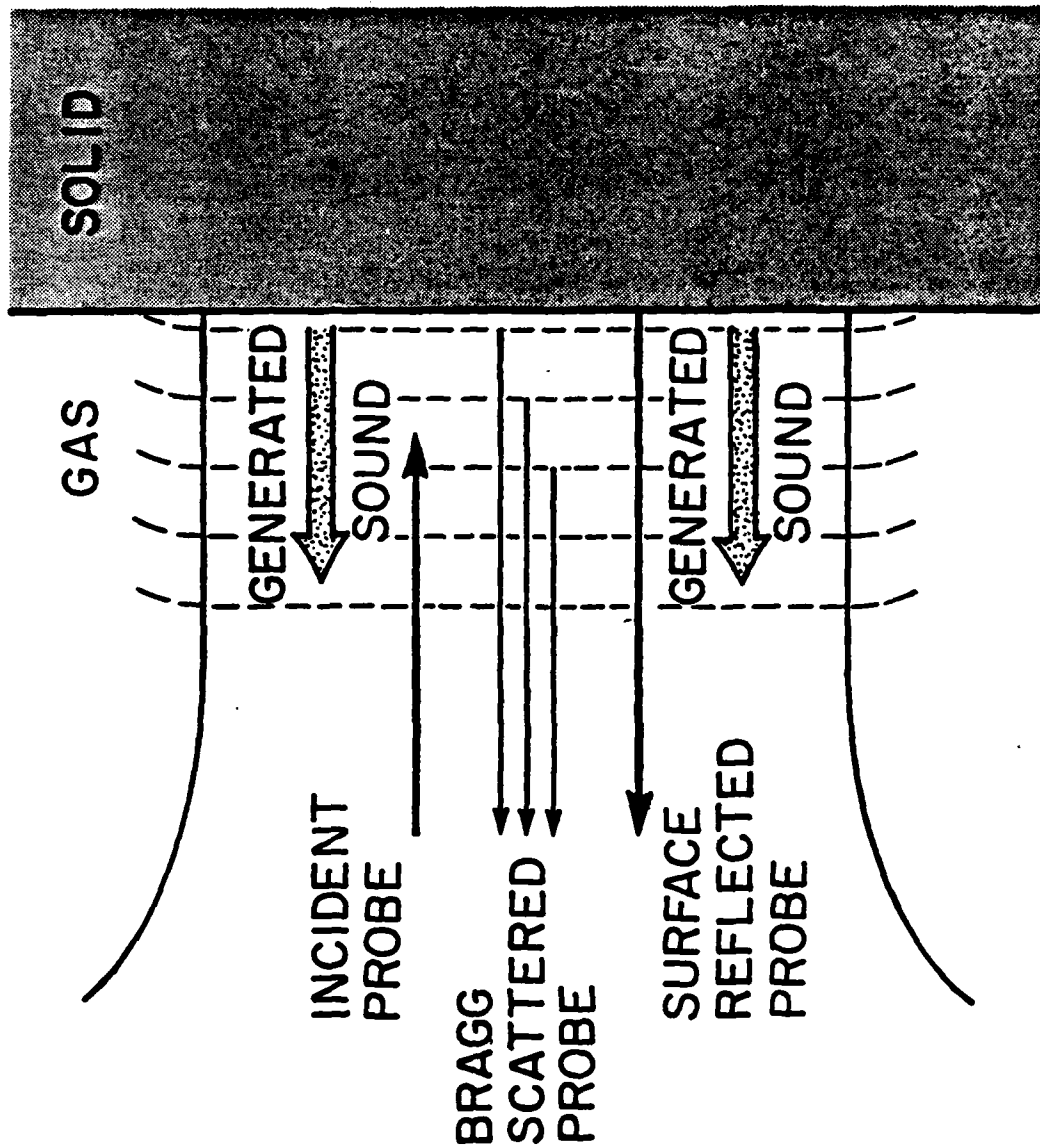


Figure 5-2. An illustration of the two reflected components of the incident probe beam. One component is reflected from the surface of the solid, while the other component is reflected and upshifted in frequency by the sound propagating in the gas.

5.2.1 Inhomogeneous Wave Equation with Acousto-optic Source Term

Starting with Maxwell's equations and the constitutive relations for an isotropic lossless medium, one obtains the familiar one dimensional traveling wave equation with a source polarization term [5.1].

$$\frac{\partial^2 \mathcal{E}}{\partial z^2} + \frac{n^2}{c^2} \frac{\partial^2 \mathcal{E}}{\partial t^2} = -\mu \frac{\partial^2 P^{NL}}{\partial t^2} \quad (5.1)$$

\mathcal{E} is the scattered electric field strength as a function of time and space, n is the index of refraction at the frequency of interest, c is the velocity of light in vacuum, μ is the permittivity, and P^{NL} is the nonlinear polarization, also a function of time and space. The scattered electric field component \mathcal{E} and nonlinear source polarization P^{NL} are defined to be of the following form.

$$\mathcal{E} = \mathcal{E}(z, t) = \text{Re}\{E e^{j(\omega t - kz)}\} \quad (5.2)$$

$$P^{NL} = P^{NL}(z, t) = \text{Re}\{P^{NL} e^{j(\omega t - kz)}\} \quad (5.3)$$

E and P^{NL} are envelope functions of \mathcal{E} and P^{NL} . Both are functions of time and space. If these definitions are substituted into the wave equation (5.1), and the slowly varying envelope approximation is employed, the result is

$$\frac{\partial E}{\partial z} + \frac{n}{c} \frac{\partial E}{\partial t} = -j \frac{1}{2} \omega \eta P^{NL}. \quad (5.4)$$

In steady state, $\partial E / \partial t = 0$, which leaves

$$\frac{\partial E}{\partial z} = -j \frac{1}{2} \omega \eta P^{NL} \quad (5.5)$$

and

$$E = \int_0^z \left(-\frac{1}{2} \omega \eta P^{NL}(z', t) \right) dz' + E(0). \quad (5.6)$$

This is the solution for the envelope function of the scattered electric field as a function of the nonlinear polarization envelope function.

5.2.2 Derivation of the Photoelastic Relation for an Ideal Gas

Before calculating the nonlinear source polarization term, the photoelastic relation in the gas must be derived. It can be obtained using the Lorentz-Lorenz formula [5.2]

$$\alpha_{pol} = \frac{3\epsilon_0(\epsilon - 1)}{N(\epsilon + 2)}, \quad (5.7)$$

where α_{pol} is the mean polarizability of the atoms or molecules, ϵ_0 is the permittivity of free space, ϵ is the relative dielectric constant, and N is the number of atoms or molecules per unit volume. For a gas, where $(\epsilon - 1)$ is much less than 1, it can be shown that

$$(\epsilon - 1) \approx \frac{N\alpha_{pol}}{MW\epsilon_0}\rho, \quad (5.8)$$

where MW is the molecular or atomic weight of the medium, and ρ is the density. The derivative of equation (5.8) provides a relation between a change in density of the gas $\delta\rho$ and the corresponding change in the relative dielectric constant $\delta\epsilon$. The result is

$$\delta\epsilon = (\epsilon - 1)\frac{\delta\rho}{\rho_0} = (\epsilon - 1)S, \quad (5.9),$$

where

$$S = \frac{\rho - \rho_0}{\rho_0} \quad (5.10)$$

is the acoustic condensation. Equation (5.9) is the photoelastic relation for an ideal gas.

5.2.3 Calculation of the Acousto-optic Nonlinear Polarization

The nonlinear polarization P^{NL} can now be calculated using the constitutive and photoelastic relations in the gas, and the two incident optical and acoustic fields, \mathcal{E}_0 and S . The constitutive relation in the gas is given by

$$P = \epsilon_0\epsilon\mathcal{E}. \quad (5.11)$$

The change in polarization $\delta\mathcal{P}$ caused by a change in the dielectric constant $\delta\epsilon$, given an electric field \mathcal{E} , is

$$\delta\mathcal{P} = \epsilon_0 \delta\epsilon \mathcal{E}. \quad (5.12)$$

The relation between acoustic condensation S and the perturbation of the dielectric constant has already been calculated in the previous section.

$$\delta\epsilon = (\epsilon - 1)S \quad (5.13)$$

Combining these results, the nonlinear polarization can be calculated.

$$\mathcal{P}^{NL} = \delta\mathcal{P} = \epsilon_0(\epsilon - 1)S\mathcal{E}. \quad (5.14)$$

The nonlinear polarization is thus proportional to the product of the incident acoustic and optical fields.

The counterpropagating acoustic and optical driving fields are defined as follows,

$$S(z, t) = \text{Re}\{S(z)e^{j(\omega_s t - k_s z)}\} \quad (5.15)$$

$$\mathcal{E}_0(z, t) = \text{Re}\{E_0(z)e^{j(\omega_0 t + k_0 z)}\} \quad (5.16)$$

where $S(z)$ and $E_0(z)$ are the slowly varying envelope functions. See Figure 5-3. Substitution of these definitions into equation (5.14) provides an expression for the non-linear source polarization.

$$\begin{aligned} \mathcal{P}^{NL} = \frac{1}{4}\epsilon_0(\epsilon - 1) & \left(S_0(z)E_0(z)e^{j[(\omega_0 + \omega_s)t + (k_0 - k_s)z]} + c.c. \right. \\ & \left. + S_0(z)^* E_0(z)e^{j[(\omega_0 - \omega_s)t + (k_0 + k_s)z]} + c.c. \right) \end{aligned} \quad (5.17)$$

Previously, this polarization \mathcal{P}^{NL} has been defined as

$$\mathcal{P}^{NL} = \mathcal{P}^{NL}(z, t) = \text{Re}\{P^{NL}e^{j(\omega t - kz)}\}. \quad (5.18)$$

Equating the two expressions requires that the envelope function P^{NL} be given by

$$\begin{aligned} P^{NL} = \frac{1}{2}\epsilon_0(\epsilon - 1) & \left(S_0(z)E_0(z)e^{j[(\omega_0 + \omega_s - \omega)t + (k_0 - k_s + k)z]} \right. \\ & \left. + S_0(z)^* E_0(z)e^{j[(\omega_0 - \omega_s - \omega)t + (k_0 + k_s + k)z]} \right). \end{aligned} \quad (5.19)$$

COLLINEAR BRAGG SCATTERING

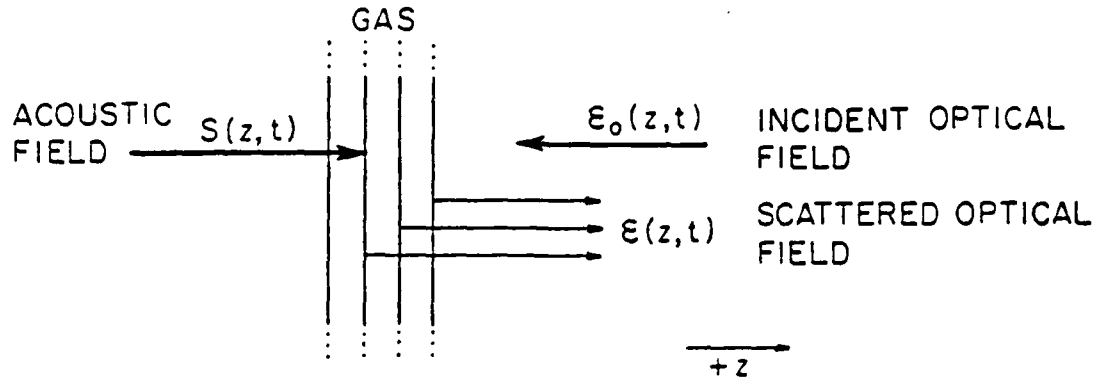


Figure 5-3 The collinear Bragg scattering geometry.

5.2.4 Bragg Scattering Efficiency

The expression for the envelope of the nonlinear source polarization P^{NL} can now be used to calculate the strength of the scattered electric field. Recall from section 5.2.1 that the scattered electric field is given by an integral of the nonlinear source polarization envelope over the interaction region.

$$E(z, t) = \int_0^z \left(-\frac{1}{2} \omega \eta P^{NL}(z', t) \right) dz' + E(0) \quad (5.20)$$

Substitution of the expression for the nonlinear polarization envelope (5.19) into this integral results in the following.

$$E(z, t) = -j \frac{1}{4} \omega \eta \epsilon_0 (\epsilon - 1) \int_0^z E_o(z') S(z') \left(e^{j[(\omega_0 + \omega_s - \omega)t + (k_0 - k_s + k)z']} + e^{j[(\omega_0 - \omega_s - \omega)t + (k_0 + k_s - k)z']} \right) dz' + E(0) \quad (5.21)$$

where $S(z)$ has been chosen to be real. This choice does not reduce the generality of the solution.

The two terms in the integrand will contribute little to the integral if the exponentials are oscillating rapidly over the slowly varying source polarization distribution. This means that for either term to significantly contribute, the k -vector sum in the exponential must be close to zero. This is what is termed as k -vector matching. See Figure 5-4.

This k -vector matching is not possible for the second term because the magnitude of k would have to be larger than the magnitude of k_0 , but the magnitude of ω would have to be smaller than the magnitude of ω_0 . This cannot occur since the k -vector magnitude is essentially proportional to frequency when there is only weak dispersion. Thus, the second term does not contribute significantly to the integral. If the k -vector mismatch is defined as

$$\Delta k = k_0 - k_s + k, \quad (5.22)$$

then the expression for the envelope of the scattered electric field is given by

$$E(z, t) = -j \frac{1}{4} \omega \eta \epsilon_0 (\epsilon - 1) e^{j(\omega_0 + \omega_s - \omega)t} \int_0^z S(z') E_0(z') e^{j\Delta k z'} dz' + E(0). \quad (5.23)$$

Under conditions of weak scattering,

$$E_0(z) \approx E_0 \quad (5.24)$$

exponential attenuation of the sound in the gas,

$$S(z) = S_0 e^{-\alpha z} \quad (5.25)$$

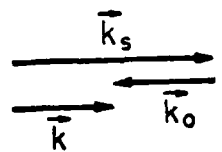
and no contribution to the scattered field for z less than zero,

$$E(0) = 0 \quad (5.26)$$

the scattered electric field strength is given by

$$E(z, t) = -j \frac{1}{4} \omega \eta \epsilon_0 (\epsilon - 1) S_0 E_0 e^{j(\omega_0 + \omega_s - \omega)t} \int_0^z e^{-\alpha z'} e^{j\Delta k z'} dz'. \quad (5.27)$$

k - VECTOR MATCHING CONDITION



$$\vec{k} = \vec{k}_s + \vec{k}_o$$

$$\omega = \omega_s + \omega_o$$

Figure 5-4. The k-vector matching condition required for collinear bragg scattering.

If γ is defined to be the following,

$$\gamma = \frac{\omega \eta \epsilon_0 (\epsilon - 1) S_0}{4\alpha} = \left[\frac{(\epsilon - 1) S_0}{2\alpha \lambda_0} \right] \quad (5.28)$$

and the k-vector matched case is assumed, $\Delta k = 0$, the envelope of the scattered electric field is given by

$$E(z, t) = -j\gamma E_0 e^{j(\omega_0 + \omega_s - \omega)t} \quad (5.29)$$

The ratio of the incident optical field to the diffracted field is given by γ , and the power diffraction efficiency Γ is just equal to the square modulus of γ .

$$\Gamma = \left| \frac{E}{E_0} \right|^2 = |\gamma|^2 = \left[\frac{(\epsilon - 1) S_0}{2\alpha \lambda_0} \right]^2 \quad (5.30)$$

This is the case for $\Delta k = 0$. If the k-vector matched case is not assumed, then the integral in equation (5.27) must be evaluated for Δk non-zero. If the integral is

evaluated at a position z far from the interaction region ($z \gg 1/\alpha$), the upper limit of the integral can be replaced by infinity without effecting the result. The integral becomes

$$\int_0^\infty e^{-\alpha z'} e^{j\Delta k z'} dz' = \left(\frac{1}{\alpha - j\Delta k} \right). \quad (5.31)$$

This is a complex Lorentzian response. The power diffraction efficiency Γ for the case of finite mismatch Δk is given by

$$\Gamma = \left[\frac{(\epsilon - 1)S_0}{2\alpha\lambda_0} \right] \frac{1}{\left(1 + \left(\frac{\Delta k}{\alpha} \right)^2 \right)}, \quad (5.32)$$

where $\Delta k = (\omega - \omega_0)/V_a$ and ω_0 is the acoustic frequency for which Δk is zero. Equation (5.32) provides a relation between the Bragg scattering efficiency Γ and the peak acoustic condensation S_0 in the gas. It also predicts a Lorentzian dependence upon the frequency of the acoustic wave in the gas.

5.3 Heterodyne Sensitivity

Since the Bragg scattered light is upshifted in frequency, detection is made possible by optically mixing it in a photodetector with the unshifted light reflected from the surface of the solid. The optical mixing provides a very sensitive means of measuring the amount of Bragg scattered light. The sensitivity is large because the heterodyne signal is proportional to the product of the signal (shifted) and reference fields (unshifted). When the reference field is large compared to the signal field, the heterodyne sensitivity can be many orders of magnitude better than direct detection of the scattered light. Furthermore, the signal can be optically mixed to a frequency where there is essentially no interference or background. To calculate the sensitivity of the probe, the noise contributed in the detection and amplification process must be taken into account. In this section, the signal to noise of the probe will be calculated as a function of the Bragg scattering efficiency.

The sensitivity of the heterodyne detection will be evaluated under the following conditions. The incident probe beam of average power P_0 is reflected

by the sound in the gas with power reflection coefficient Γ , and reflected from the sample surface with power reflection coefficient R . Both reflected components propagate collinearly back to the photodetector where they generate a heterodyne signal at the frequency of the acoustic wave in the gas. The optical heterodyne power is proportional to the product of the fields from these two reflections. The peak optical heterodyne power at the acoustic frequency (w_a) is given by

$$P_{het} = 2\sqrt{RP_0}\sqrt{\Gamma P_0} = 2\sqrt{R}\sqrt{\Gamma}P_0. \quad (5.33)$$

Conversion of the optical heterodyne power to an RF signal takes place in the photodetector. The peak heterodyne current is given by

$$I_{het} = \alpha_r P_{het}, \quad (5.34)$$

where α_r is the responsivity (amps/watt) of the photodetector. The average signal power into the load resistor is thus given by

$$P_{signal} = \frac{1}{2} I_{het}^2 R_l = 2\alpha_r^2 R \Gamma P_0^2 R_l. \quad (5.35)$$

There are three sources which contribute noise to the signal as it is detected and amplified. They are shot noise, Johnson noise, and amplifier noise. The total noise power contributed by these three sources is given by [5.3,5.4]

$$P_{noise} = 4KTBF + 2e\alpha_r BRP_0 R_l, \quad (5.36)$$

where K is the Boltzman's constant, T is the absolute temperature, B is the bandwidth, F is the noise figure of the preamplifier, e is the electron charge, α_r is the detector responsivity (A/W), R_l is the load resistance, and P_0 is the average detected power. Thus the signal-to-noise ratio is given by

$$\frac{S}{N} = \frac{2\alpha_r^2 R \Gamma P_0^2 R_l}{4KTBF + 2e\alpha_r BRP_0 R_l}. \quad (5.37)$$

This equation establishes the relationship between the signal to noise ratio and the Bragg scattering efficiency Γ , given the other detection system parameters.

One interesting point about the Bragg interaction must be made. After the incident probe beam is reflected from the surface of the solid, it sees another traveling acoustic wave. The Bragg condition is met once again for back scattering. However, the frequency in this case is down shifted because the sound wave is receding from the solid. The down shifted light propagates back to the solid, where it is reflected, and then propagates away with the upshifted light. The result is a double sidebanded carrier. The phase relation between the upper and lower side band relative to the carrier is identical to that found when phase modulation takes place. The distinguishing feature, however, is that the lower sideband has gone through two reflections from the surface of the solid. Since the reflectivity of the solid will always be less than one, the amplitude of the lower sideband will always be less than the upper sideband by a factor of R , the power reflectivity of the solid. The heterodyne signal, with this effect included, is now proportional to the difference between the sideband amplitudes rather than the amplitude of the single sideband. To include this effect in the signal to noise ratio calculation, the reflectivity in the numerator of equation (5.37) must be replaced by the following expression.

$$R - R(1 - R)^2 \quad (5.38)$$

One of the attractive features of this heterodyne scheme is that an interferometer is not required to detect of the signal. This is the result of the fact that the sidebands on the carrier do not have equal amplitudes. In contrast, techniques which rely on phase modulation of an optical carrier, such as displacement interferometry, must use a reference local oscillator which is in quadrature with the center carrier for demodulation. These techniques generally require a stabilized interferometer.

There may be circumstances where the use of an interferometer arrangement with the Bragg detection may be desirable. In cases where the surfaces are rough or highly absorbing, there would be advantage to using a reference which did not depend upon the surface reflectivity of the material being imaged. In these cases,

the probe beam could be split, a portion sent into the cell to be Bragg scattered by the sound propagating in the gas, and the rest sent to the reference arm of the interferometer. The reflection from the sound propagating in the gas could then be mixed with the reference beam and a signal obtained independent of the reflectivity of the solid. Under these circumstances, the signal to noise ratio would be given by equation (5.37), without the dependence upon the sample reflectivity. In most cases, however, the disadvantages of using a stabilized interferometer outweigh the problems of having a signal which is dependent upon the reflectivity of the sample surface.

5.4 Thermoacoustic Generation of Sound

When the surface temperature of a solid varies harmonically with time, a periodic temperature distribution is generated in the surrounding gas. This temperature distribution couples to an acoustic wave through the expansion of the gas. If the amount of sound generated by the expansion of the gas is large compared to the sound generated by the thermally generated displacement of the solid, then a measurement of the sound in the gas is equivalent to a measure of the ac surface temperature of the solid.

A simple one dimensional analysis can be used to determine under what conditions the contribution of the gas will be large compared to the contribution of the solid. The surface displacement of a solid when periodically heated at its surface can be shown to be approximately equal to [5.5]

$$U_s = \alpha_s \theta_0 \lambda_{ts}, \quad (5.39)$$

where α_s is the linear coefficient of expansion of the solid, θ_0 is the peak sinusoidal temperature variation at the surface of the solid, and $\lambda_{ts} = \sqrt{(2\kappa_s/\omega)}$ is the thermal wavelength in the solid. This surface displacement U_s causes an equal displacement in the gas, since the acoustic displacement at the interface must be continuous. In addition, the thermal expansion of the gas generates a displacement in the gas

which is given by

$$U_g = \alpha_g \theta_0 \lambda_{tg}, \quad (5.40)$$

where the same definitions as above apply for the gas. Since the acoustic power density is proportional to the square of the displacement, the ratio squared of the two displacements gives the relative amount of power contributed by the expansion of gas as compared with the expansion of the solid.

$$\frac{P_g}{P_s} = \left| \frac{U_g}{U_s} \right|^2 = \frac{\alpha_g^2 \kappa_g}{\alpha_s^2 \kappa_s} \quad (5.41)$$

Table 5-1 below shows the relative power contribution of argon gas at a pressure of 100 atmospheres as compared with several solids.

TABLE 5-1

Relative Source Strength of Acoustic Power in the Gas

	Silicon	Fused Quartz	Gold	Aluminum
Exp. Coeff. (α_s)	2.5×10^{-6}	5.5×10^{-7}	1.3×10^{-5}	2.3×10^{-5}
Diffusivity (κ)	1.0×10^{-4}	8.3×10^{-7}	1.3×10^{-4}	9.6×10^{-5}
Power ratio (P_g/P_s)	4.3×10^2	1.1×10^6	1.2×10^1	5.33

*References [5.6,5.7]

As can be seen from the table, for many materials, the amount of acoustic power in the gas is essentially determined only by the temperature fluctuation at the surface of the solid.

When the optical absorption depth L_{opt} is finite, the calculation shown above must be modified. Under this condition, the displacement ratio is approximated by the following expression.

$$\frac{U_g}{U_s} = \frac{\alpha_g \lambda_{tg}}{\alpha_s (\lambda_{ts} + L_{opt})} \quad (5.42)$$

In silicon, where the optical absorption depth is approximately 4000 Å for green light, the power contributed by the gas is nearly two orders of magnitude larger than that contributed by the solid.

Since the acoustic power in the gas is essentially determined by the harmonic temperature at the surface of the solid, a relationship can be established between this temperature and the acoustic condensation in the gas. Because the acoustic impedance of the solid is much larger than that of the gas, the thermoacoustic generation of sound in the gas can be considered to be under constrained boundary conditions. Using the formalism from Chapter 3, the acoustic condensation generated thermoacoustically in the gas can be shown to be

$$S_0 = \frac{k_a \alpha_g \theta_0}{k_t}, \quad (5.43)$$

where k_a and k_t are the acoustic and thermal k-vectors in the gas, α_g is the expansion coefficient of the gas, and θ_0 is the peak ac temperature rise at the surface of the solid. This provides a relationship between the magnitude of the sinusoidal surface temperature of the solid θ_0 and the magnitude of the acoustic condensation in the gas S_0 . This result can now be used to relate the Bragg scattering efficiency, derived in section 5.2.4, to the harmonic surface temperature of the solid.

5.5 Photothermal Sensitivity

Using the results from the three previous sections, the photothermal sensitivity of the probe can be calculated. Combining equation (5.30) from section 5.2 and equation (5.43) from the previous section, the Bragg scattering efficiency Γ under phase matched conditions can be related to the harmonic surface temperature θ_0 .

$$\Gamma = \left[\frac{\pi(\epsilon - 1)S_0}{2\alpha\lambda_0} \right]^2 = \left[\frac{\pi(\epsilon - 1)}{2\alpha\lambda_0} \right]^2 \left(\frac{k_a \alpha_g}{k_t} \right)^2 \theta_0^2 \quad (5.44)$$

If this relation is substituted into equation (5.37) of section 5.3,

$$\frac{S}{N} = \frac{2\alpha_r^2 R \Gamma P_0^2 R_l}{4K T B F + 2e\alpha_r B R P_0 R_l} \quad (5.45)$$

an expression is obtained for the signal to noise ratio as a function of the harmonic surface temperature of the solid.

$$\frac{S}{N} = \left(\frac{2\alpha_r^2 R P_0^2 R_l}{4K T B F + 2e\alpha_r B R P_0 R_l} \right) \left[\frac{\pi(\epsilon - 1)}{2\alpha\lambda_0} \right]^2 \left(\frac{k_a \alpha_g}{k_t} \right)^2 \theta_0^2 \quad (5.46)$$

This characterizes the photothermal sensitivity of the probe. Table 5-2 contains the experimental conditions under which this sensitivity will be evaluated.

TABLE 5-2

Experimental Conditions - Argon gas (100 atm., 300 °K)

Detector responsivity	α_r	.33 A/W
Sample reflectance	R	.5
Incident Optical Power	P_0	5.0 mW
Load Resistor	R_l	50 Ω
Boltzman constant	K	$1.38 \times 10^{-23} J/^{\circ}K$
Temperature	T	300 °K
Noise figure	F	1.77 (2.5 db)
Optical wavelength	λ_0	632 nm
Dielectric constant	ϵ	1.055
Acoustic atten. const.	α	$1.7 \times 10^5 /m$
Acoustic k-vector (1.03 GHz)	k_a	$1.98 \times 10^7 /m$
Linear expansion coeff.	α_g	1.11×10^{-3}
Thermal k-vector (1.03 GHz)	k_t	$1.2 \times 10^8 /m$

With these values, the photothermal sensitivity is given by

$$\frac{S}{N} = \left(\frac{6.9 \times 10^7}{B} \right) \theta_0^2 \quad (5.47)$$

In a 1 Hz bandwidth, the minimum detectable harmonic temperature variation is given by

$$\theta_{min} = 1.2 \times 10^{-4} {}^{\circ}C \quad (5.48)$$

This sensitivity compares very favorably with the sensitivities of other techniques, as will be shown in section 5.7. Furthermore, this temperature variation need not occur over a region larger than the optical probe spot size.

5.8 Acousto-optic Coupling Medium - Figure of Merit

In the previous section, a relation was established between the signal to noise ratio and the ac temperature at the solid surface given the optical, electrical and physical properties of the detection system. This relation was then used to calculate the photothermal sensitivity, with argon gas as the acousto-optic coupling medium. Although argon gas is very attractive as an acousto-optic coupler, many other gases and liquids could potentially be used to couple the photothermally generated sound to the probe beam. In this section, a figure of merit for the coupling medium will be derived from equation (5.46) of the previous section and various liquids and gases will then be evaluated for use in the photothermal laser probe.

The sensitivity of the photothermal probe depends upon the characteristics of the acousto-optic coupling medium through the following parameters: the dielectric constant ϵ , acoustic attenuation constant α , acoustic velocity V_a , linear expansion coefficient α_g , and thermal diffusivity κ . A figure of merit can be defined using these parameters in such a way as to make possible the relative evaluation of different acousto-optic coupling media. The signal to noise ratio calculated in the previous section is proportional to the properties of the coupling medium in the following way.

$$\frac{S}{N} \propto \frac{(\epsilon - 1)^2 \alpha_g^2 \kappa}{(\frac{\alpha}{f^2})^2 V_a^3} \quad (5.48)$$

A figure of merit is obtained if the right side of this equation is normalized by the signal to noise ratio obtained with a reference medium: argon gas at a pressure of 100 atmospheres.

$$F.M. = (8.9 \times 10^6) \frac{(\epsilon - 1)^2 \alpha_g^2 \kappa}{(\frac{\alpha}{f^2})^2 V_a^3} \quad (5.49)$$

Below is found a table of several different gases and liquids with their associated

figure of merit as calculated using equation (5.49).

TABLE 5-3

Acousto-optic Coupling Media

Media	Bragg Freq. (GHz)	Figure of Merit
Argon gas (100 atm.)	1.03	1.0
Argon liquid (87 °K)	2.7	360.
Nitrogen liquid (77 °K)	2.7	4.7
Helium liquid (4.2 °K)	0.57	150
Water (300 °K)	4.9	0.12
Air (300 °K, 1 atm.)	1.0	10^{-6}

As can be seen, there are reasons for using cryogenic liquids as the coupling media. This may be especially interesting for evaluating crystalline defects and doping in silicon or other semiconductors. At room temperature, the thermal conductivity of silicon is almost independent of the defect concentration unless the density is greater than $10^{18}/\text{cm}^3$ [5.8]. The reason for this is that the dominant phonon scattering mechanism at room temperature is three phonon scattering or umklapp scattering. Only at lower temperatures is the scattering dominated by impurity scattering. Theory predicts that with liquid argon (87 °K) as the coupling liquid, dopant concentrations in silicon should be measurable down to levels near $10^{16}/\text{cm}^3$. Furthermore, the sensitivity of the probe is enhanced by more than two orders of magnitude by the use of liquid argon rather than the high pressure gas. Working with liquid argon would also require that a higher pump beam modulation frequency be used as is shown in Table 5-3.

5.7 Comparison of Photoacoustic and Photothermal Techniques

It is difficult to make a direct comparison of many of the available photothermal and photoacoustic techniques due to the wide range of applications, resolution requirements and frequencies employed. There are several high resolution techniques,

however, that can be evaluated and compared in a clear way when performing a specific function. The three techniques that will be compared are photodisplacement interferometry, photoacoustic detection with an acoustic lens, and photothermal Bragg detection. The comparison can be made by calculating for each technique the smallest harmonic temperature variation at the surface of a solid that can be detected within a given bandwidth. The evaluation will be made at a frequency of 1 GHz, since the photothermal Bragg detection is locked at this frequency by the Bragg resonance. After calculation of the individual sensitivities of these three techniques, the results will be discussed and compared.

To determine the sensitivity of photothermal displacement interferometry, a periodic temperature at the surface of a solid must be related to the thermoacoustically generated displacement. Then using published values of displacement sensitivity, the sensitivity to periodic temperature can be calculated.

If a solid is periodically heated at its surface, the resultant harmonic temperature varies over a region of approximately one thermal wavelength. The resultant surface displacement is given approximately by [5.5]

$$U_s = \theta_0 \alpha_s \lambda_{ts}, \quad (5.50)$$

where θ_0 is the peak harmonic temperature, α_s is the linear expansion coefficient, and λ_{ts} is the thermal wavelength at the frequency of the harmonic temperature. This provides the relation between harmonic temperature and surface displacement. The minimum detectable surface displacement with interferometry has been reported as 3×10^{-4} Å with a 0.1 second integration time [5.9]. The displacement sensitivity is therefore given by

$$U_{min} = \frac{10^{-4} \text{Å}}{\sqrt{Hz}}. \quad (5.51)$$

The combination of the two previous relations provides a photothermal sensitivity for displacement interferometry.

$$\theta_{min} = \frac{10^{-4} \text{°C}}{\alpha_s \lambda_{ts} \sqrt{Hz}} \quad (5.52)$$

For the case of the acoustic lens, the surface displacement must be converted to an acoustic power density in the coupling liquid. The assumption is made that the acoustic loading of the surface displacement by the coupling liquid is small. This is a good approximation because the impedance of most liquids is very small compared to the impedance of solids. Without loading, the power density in the liquid created by the displacement of the solid is given by

$$\frac{P}{A} = \frac{1}{2} Z_l \omega^2 U_s^2, \quad (5.53)$$

where Z_l is the acoustic impedance of the liquid and ω is the radian frequency of the modulation. Using equation (5.50), this power density can be related to the surface temperature of the solid.

$$\frac{P}{A} = \left(\frac{1}{2} Z_l \omega^2 \alpha_s^2 \lambda_{ts}^2 \theta_0^2 \right) \quad (5.54)$$

The total acoustic power generated by this periodic temperature over a given area is

$$P = \left(\frac{P}{A} \right) (Area). \quad (5.55)$$

The photothermal sensitivity for the acoustic lens can now be calculated using the results of section 4.3. If the acoustic detection efficiency of the lens is near 10^{-2} , and the noise is given by $10^{-20}/B$ Watts-sec, the minimum detectable acoustic power at the focus is approximately given by

$$P_{min} = \frac{10^{-18}}{Hz} \text{ Watts-sec}. \quad (5.56)$$

The photothermal sensitivity of the acoustic lens is therefore given by

$$\theta_{min} = \sqrt{\frac{2P_{min}}{Z_l Area}} \left(\frac{1}{\omega \alpha_s \lambda_{ts}} \right) ^\circ C. \quad (5.57)$$

The expressions for the photothermal sensitivity of interferometry and acoustic lens techniques will now be evaluated using material values for silicon and a one square micrometer area. Under these conditions, the minimum detectable harmonic

temperature for the interferometric technique is given by

$$\theta_{min} = \frac{2.2 \times 10^{-2} C}{\sqrt{Hz}}. \quad (5.58)$$

The photothermal sensitivity of the acoustic lens is given by

$$\theta_{min} = \frac{4.1 \times 10^{-4} C}{\sqrt{Hz}}. \quad (5.59)$$

The sensitivity of Bragg detection was calculated in section 5.5. The result was

$$\theta_{min} = \frac{1.2 \times 10^{-4} C}{\sqrt{Hz}}. \quad (5.60)$$

Comparing these sensitivities, it is clear that for the case of silicon, the Bragg detection compares favorably with the other techniques. Because the photothermal sensitivity of the interferometric and acoustic lens techniques depend upon the expansion coefficient and thermal wavelength, the relative sensitivities will depend upon the material being examined. However, two points must be made. First, it can be shown that the acoustic lens technique will always remain more sensitive than the interferometry. Second, it can be shown that the photothermal sensitivity of Bragg detection will always be much greater than that of displacement interferometry if the pressure of the argon gas is greater than 120 atmospheres.

5.8 Experimental Verification of the Theory

5.8.1 Experimental Implementation

A schematic diagram of the photothermal surface probe is shown in Figure 5-5. A pump laser, modulated at 1.03 GHz, is focused by an optical microscope objective (9) inside the gas cell to a diffraction limited spot on the sample surface (10). The absorbed optical power photothermally generates sound which propagates away from the solid. The probe laser is directed through a quarter wave plate (7) into the cell by a partial mirror (3), and a polarizing beam splitter (6), where it is focused to the same location as the pump beam. There, it is reflected at

EXPERIMENTAL SET-UP

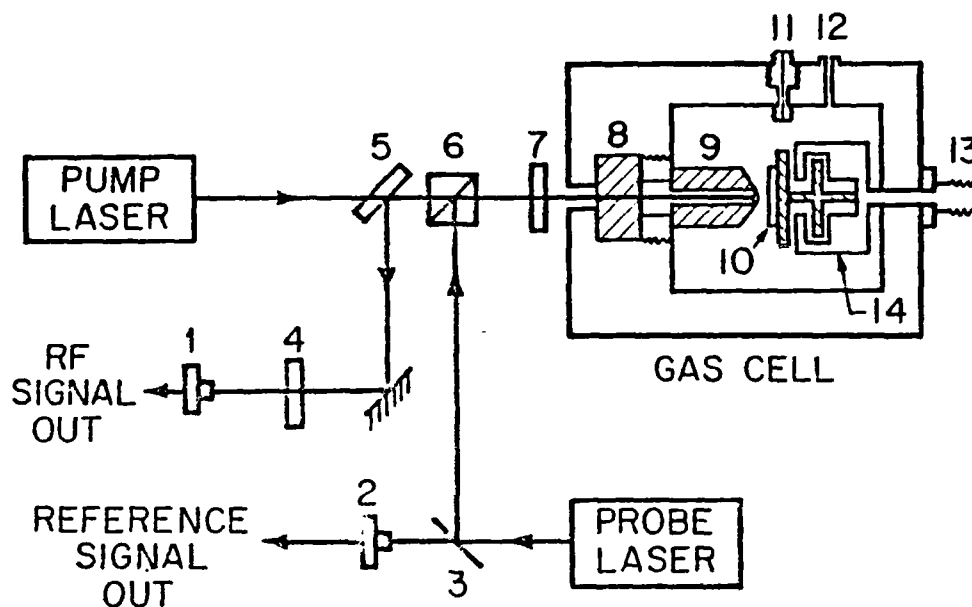


Figure 5-5. Experimental Arrangement. (1),(2) fast silicon photodiodes; (3) beamsplitter; (4) spike interference filter; (5) diroic mirror; (6) polarizing beamsplitter; (7) quarter wave plate; (8) optical window; (9) focusing objective; (10) sample; (11) electrical feed through; (12) gas input; (13) focusing micrometer; (14) electro-mechanical scanner.

the sample surface as well as by the sound wave propagating in the gas. These two reflected components are then recollimated by the optical objective, and pass through the quarter wave plate a second time. The two passes through the quarter wave plate cause a 90 degree rotation of the polarization. The reflected probe therefore propagates through the polarizing beam splitter. It is then reflected by a dichroic mirror (5) and finally passes through a narrow band interference filter (4) to a fast photodiode (1). The interference filter isolates the photodiode from the pump laser power. The cell is pressurized to 50-100 atmospheres by simply connecting it through a high pressure regulator to a standard argon gas cylinder. The sample is positioned at the focus by a micrometer (13) from outside the gas cell. An electro-mechanical scanner [5.10] (14) inside the gas cell makes possible two dimensional scanning of the sample with respect to the pump and probe beams. A reference signal at the frequency of the axial mode spacing of the probe laser (ω_r) is detected in a second photodetector (2).

To avoid the problems of RF interference that occur when detecting at the modulation frequency of the pump laser (ω_a), the two longitudinal modes of the He-Ne probe laser are used to optically mix the heterodyne signal to a frequency other than that of the acoustic wave. This is accomplished by optically mixing the Bragg shifted signal from one axial mode ($\omega_o + \omega_a$) with the unshifted second axial mode ($\omega_o + \omega_r$). The result is a heterodyne signal out of the optical detector at the difference between the acoustic frequency and the axial mode spacing ($\omega_a - \omega_r$). This signal is then mixed down to an IF frequency, filtered and square law detected. See Figure 5-6. For phase sensitivity, the signal can also be mixed down to dc and detected with a lock-in amplifier.

5.8.2 Frequency Dependence

The frequency dependence of the Bragg interaction was measured in the following way. A small portion of the pump beam was split off and the modulated optical power was monitored using a fast photodetector and an RF spectrum analyser. While changing the modulation frequency of the pump, the signal from

DETECTION ELECTRONICS

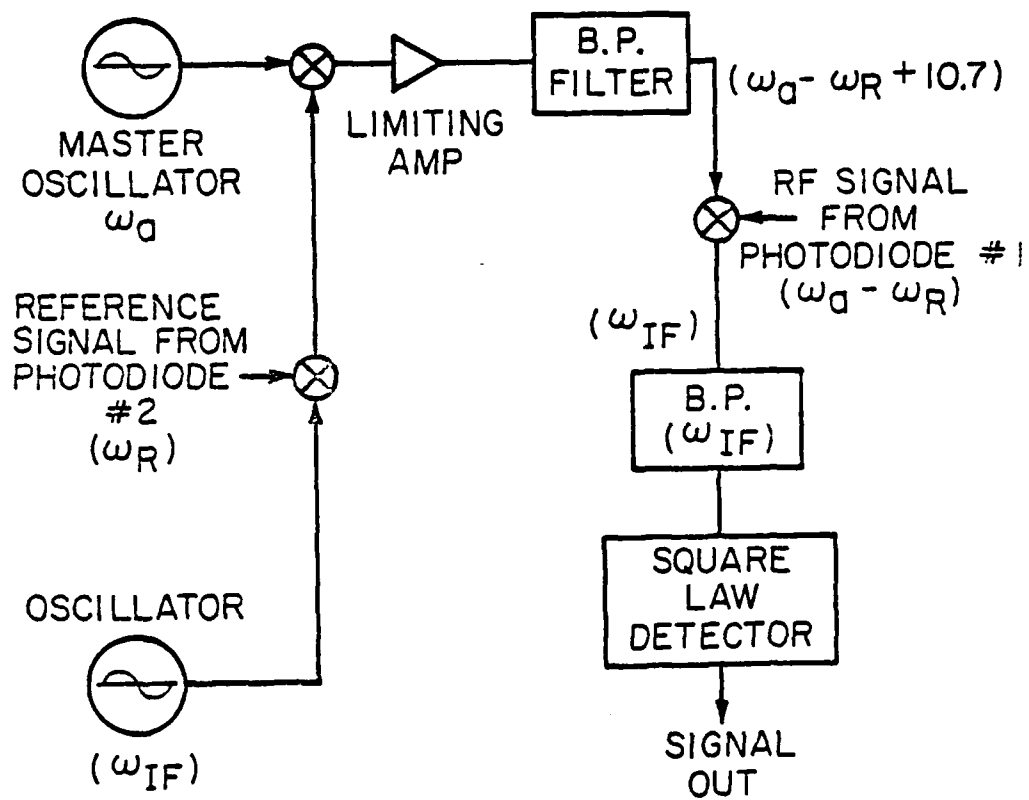


Figure 5-6. Heterodyne detection system.

the probe beam was measured. The probe signal was then normalized by the modulated pump power as measured with the photodiode and spectrum analyser. The experimental results are shown with the theoretically expected Lorentzian frequency dependence in Figure 5-7.

5.8.3 Absolute Sensitivity

The absolute sensitivity of the probe to acoustic power was measured using a 1 GHz acoustic flat as the source of sound in the gas. The acoustic flat was chosen to measure the sensitivity for two reasons. First, the flat provides a fairly uniform acoustic power density over a relatively large area ($10^4 \mu\text{m}^2$). This makes the positioning of the probe beam a relatively simple task. The second reason is that it is possible to calculate the acoustic power density in the gas transmitted from the flat by measuring the RF input power and the insertion loss using a pulse echo technique. Measurement of the insertion loss of the transducer and calculation of the transmission of the sound from the flat into the gas determines the total acoustic power in the gas. The acoustic spot size can be calculated from the size of the transducer. This information provides a knowledge of the acoustic power density in the gas. To avoid any miscalculation due to a resonance of the flat itself, the insertion loss measurements were made using acoustic pulses which were shorter than the round trip time in the flat.

To locate the region illuminated by the acoustic power on the front surface of the flat, the flat was illuminated by a focused modulated laser. The flat was scanned with respect to the laser spot, and an image was obtained of the photoacoustic sound detected by the flat in receiving mode. A scanned optical reflection image was also obtained of the same region. Comparison of the two images identified the region where the acoustic illumination was to be found. The acoustic spot diameter was approximately $100 \mu\text{m}$. The optical image was then used to locate this region for positioning of the probe beam. Below are found the experimental conditions and the minimum detectable acoustic intensity I_{min} in the gas.

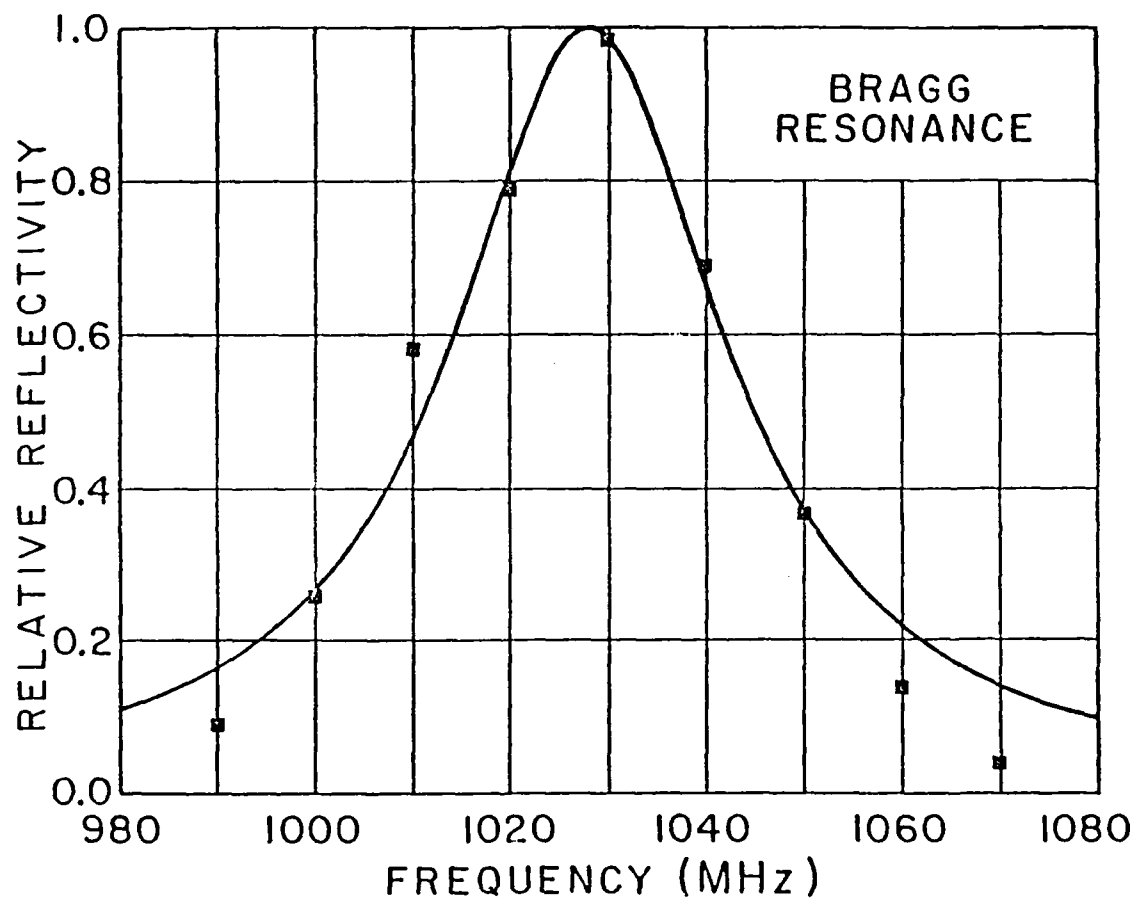


Figure 5-7. The theoretically predicted collinear Bragg scattering efficiency as a function of the frequency of the sound in the gas with the experimental data.

AD-A150 823

PHOTOACOUSTIC IMAGING(U) STANFORD UNIV CA EDWARD L
GINZTON LAB OF PHYSICS C C WILLIAMS ET AL. OCT 84
GL-3777 AFOSR-TR-85-0124 AFOSR-82-0248

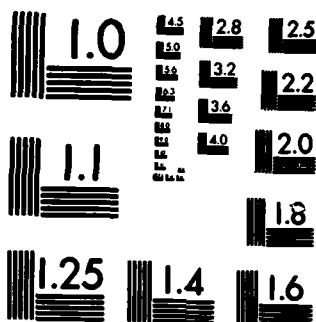
2/2

UNCLASSIFIED

F/G 14/5

NL





MICROCOPY RESOLUTION TEST CHART
NATIONAL BUREAU OF STANDARDS-1963-A

$$P_{gas} = 50 \text{ atmospheres}$$

$$P_0 = 1.75 \text{ mW}$$

$$R_{eff} = .04$$

$$F = 1.77$$

$$B = 5 \text{ MHz}$$

$$R_l = 50 \Omega$$

$$I_{min} = 5.5 \times 10^4 \text{ W/m}^2$$

A calculation of the theoretical sensitivity to acoustic power in the gas using the experimental values above indicates that the experimental sensitivity is a factor of 3.5 less than that predicted by theory. This value is not much larger than the combined experimental uncertainty in the measurement.

5.8.4 Dependence on Pressure

Using the same experimental arrangement described in the previous section, the pressure of the gas was varied as the measurement was made. The results showed that the signal was proportional to the pressure to a power of 2.5 over a range of 26 to 66 atmospheres.

$$S \propto P_{gas}^{2.5} \quad (5.61)$$

The theory predicts that the signal should vary as the third power of the pressure of the gas [5.11].

The most plausible explanation of the discrepancy between the theory and experiment is the following. Since the probe beam is highly focused and the sound delivered by the acoustic flat is essentially planar, the phase fronts of the two fields are most closely matched in the region near the focus. Farther from the focus, the spherical phase curvature on the optical beam makes efficient heterodyning impossible due to the mismatch in the phase curvature between the scattered and reference beams. At low pressures, the acoustic attenuation is high, so the only region which contributes to the heterodyne signal is near the focus. As the pressure is increased, the regions farther from focus begin to contribute. However, due to

the mismatch in the spacial phase fronts, they do not contribute as much as would be predicted by theory which assumes perfectly matched phase fronts. This could explain why the measured pressure dependence goes to a power of 2.5 rather than 3.0.

5.9 Photothermal Imaging of Implanted Silicon

To demonstrate the sensitivity of the probe to variations in the thermal properties of materials, a silicon wafer was implanted with 150 KeV boron through a resist pattern [5.12]. After implantation, the patterned resist was plasma etched, leaving only a thin oxide. This oxide was then removed, exposing a clean silicon surface. Thus, the silicon was left uniformly implanted, except in the regions where the resist had isolated the silicon from the boron implant. In these regions, the silicon was intrinsic. The implant density was calculated to be $10^{18}/\text{cm}^3$ at the surface, increasing to $10^{21}/\text{cm}^3$ at a depth of 5000 Å.

The sample was imaged with the photothermal probe, and there was found a variation in the thermal response of the implanted region (darker) relative to the unimplanted region (lighter). The photothermal image is shown in Figure 5-8(a). The spacing of the II-like characters from center to center is approximately 15 microns. A 3% variation in the optical reflection was measured from region to region due to the effects of the implantation. This optical variation is too small to account for the photothermal contrast seen in the image. However, to eliminate any optical variation, 300 Å of titanium were deposited on the silicon surface and the sample was imaged again. Figure 5-8(b) again shows the thermal contrast due to the boron implant. The titanium covered silicon region (left) actually generates a larger photothermal signal than the silicon alone. This is largely due to the greater optical attenuation constant of the titanium. The signal from the uncoated silicon region (right) is not apparent in the image because the bias level and gain of the signal were adjusted to allow for maximum contrast in the titanium/silicon region. The source of contrast in the titanium covered silicon region is the variation in the thermal wave reflectance at the interface between the titanium and silicon. These images clearly demonstrate the sensitivity of the probe to changes in the thermal properties of the silicon created by the boron implantation.



(a)

10 μm



(b)

10 μm

Figure 5-8. (a) Photothermal image of boron implanted silicon. The darker area is the implanted region, the lighter region is not implanted. (b) Photothermal image of implanted silicon with 300 Å of titanium deposited on the silicon in the left half of the image.

5.10 Summary

The theory behind the photothermal laser probe has been presented along with an experimental verification of the theory. The sensitivity has been shown to compare favorably with other high resolution techniques. A figure of merit has been defined and several coupling media have been evaluated. High resolution images have been obtained demonstrating the resolution and sensitivity of the probe to variations in the thermal properties of materials.

The features which distinguish this photothermal probe from other techniques are the high frequency of modulation, the non-contacting nature of the evaluation and the high sensitivity to ac temperature variations over very small areas. In applications where the highest sensitivity and resolution is desired, the probe should provide a unique tool for materials evaluation.

The possibilities for application of the probe to useful materials characterization problems have barely been investigated. Future effort is planned in this area. There are several materials and systems for which the probe appears well suited. Examples of such materials are polycrystalline materials with anisotropic grains, very thin transparent films on absorbing substrates, and semiconductor surfaces. Another area of future interest is the use of the cryogenic liquids as coupling media for the evaluation of semiconductors at low temperatures. It is expected that the probe will provide new and useful information in all of these applications.

References for Chapter 5

- [5.1] Amnon Yariv, *Quantum Electronics*, New York: John Wiley and Sons, 1975, p. 356.
- [5.2] M. Born and E. Wolf, *Principles of Optics*, Oxford: Pergamon Press, 6th Ed., 1980, p. 87.
- [5.3] R. L. Whitman and A. Korpel, "Probing of Acoustic Surface Perturbations by Coherent Light," *Appl. Opt.* **8**, 1567 (1969).
- [5.4] R. M. De La Rue, R. F. Humphryes, I. M. Mason, and E. A. Ash, "Acoustic-surface-wave amplitude and phase measurements using laser probes," *Proc. IEE* **119**, 117 (1972).
- [5.5] R. M. White, "Generation of Elastic Waves by Transient Surface Heating," *J. Appl. Phys.* **34**, 3559 (1963).
- [5.6] David White, "Critical Constants," p. 4-33; George T. Furukawa and Thomas B. Douglas, "Heat Capacities," p.4-105; Richard K. Kirby, Thomas A. Hahn, and Bruce D. Rothrock, "Thermal Expansion," p. 4-19; Robert L. Powell and Gregg E. Childs, "Thermal Conductivity," p.4-142; *AIP Handbook*, Third Edition, Dwight E. Gray ed., New York: McGraw-Hill, 1972.
- [5.7] *Handbook of Chemistry and Physics*, Robert C. Weast, ed., Cleveland: CRC Press, 1975 p. F-78.
- [5.8] S. Holland and R.M. White, "Concentration Dependence of Thermal-wave Contrast for Dopants in Silicon," *1983 Ultrasonics Symposium Proc.*, Atlanta, Georgia, 1983, p. 681.
- [5.9] J. E. Bowers, "Fiber-Optic Sensor for Surface Acoustic Waves," *Appl. Phys. Lett.* **41**, 231 (1982).
- [5.10] J. Heiserman, D. Rugar, and C. F. Quate, "Cryogenic Acoustic Microscopy," *J. Acoust.Soc. Am.* **67**, 1629 (1980).

- [5.11] C.C. Williams, "High Resolution Acousto-optic Laser Probe," *1983 Ultrasonics Symposium Proc.*, Atlanta, Georgia, 1983, p. 952.
- [5.12] Courtesy of L. Moberly, National Semiconductor, Santa Clara, California 95051.

Appendix

\$WATFIV

C THIS PROGRAM CALCULATES THE AC AND DC TEMPERATURE RESPONSE
C AT THE SURFACE OF AN ISOTROPIC SEMI-INFINITE ABSORBING SOLID
C WHEN ILLUMINATED BY AN INTENSITY MODULATED GAUSSIAN. OPTICAL
C BEAM.

C

C

C DIMENSION VARIABLES AND ARRAYS

C

C DEFINITION OF VARIABLES

C

C W = 1/e HALF WIDTH OF OPTICAL FIELD

C KAPPA = DIFFUSIVITY OF SOLID

C ALPHA = POWER ABSORPTION CONSTANT OF SOLID

C F = POWER MODULATION FREQUENCY

C KTHERM = THERMAL K VECTOR

C PNOT = TOTAL POWER IN OPTICAL BEAM

C INOT = INTENSITY AT CENTER OF GAUSSIAN BEAM

C PPV = ABSORBED OPTICAL POWER PER UNIT VOLUME

C GRIDAB = SIZE OF THE RADIAL GRID ELEMENT

C GRIDC = SIZE OF THE Z GRID ELEMENT

C VE = VOLUME OF EACH ELEMENT IN SUMMATION

C NAB = NO. OF THERMAL WAVELENGTHS SUMMED OVER IN RADIAL DIRECTION

C NC = NUMBER OF THERMAL WAVELENGTHS SUMMED OVER IN Z.

C RES = RESOLUTION FACTOR OF INTEGRATION GRID

C TEMP(1) = SUM OF AC TEMPERATURE CONTRIBUTIONS

C TEMP(2) = SUM OF DC TEMPERATURE CONTRIBUTIONS

C TEMPM1 = MAGNITUDE OF AC TEMP VARIATION

C TEMPM2 = MAGNITUDE OF DC TEMP VARIATION

C THCON = THERMAL CONDUCTIVITY OF SOLID

C RHO = DENSITY OF SOLID

C CAP = HEAT CAPACITY OF SOLID

C KAPPA = THCON/RHO*C

C AAB,CC ARE DUMMY INTEGRATION VARIABLES

C AB,C ARE ACTUAL VALUES OF POSITION CORRESPONDING TO AA,BB,CC

C ABMAX,CMAX ARE UPPER LIMITS OF AAB,CC AS DETERMINED BY

C THE GRID SIZE AND REGION OVER WHICH THE INTEGRATION WILL OCCUR.

C

C DIMENSION VARIABLES

```

C
COMPLEX*16 TEMP(2), K THERM
INTEGER AAB, CC, ABMAX, CMAX, RES
REAL*8 KAPPA, INOT, L THERM, GRIDAB(2), GRIDC(2)

C
C      READ IN PARAMETERS
C
      READ (5,*) PNOT, W, F, ALPHA
      READ(5,*) THCON, RHO, CAP
      READ (5,*) NAB, NC, RES
      KAPPA = THCON/(RHO*CAP)

C
C      OUTPUT PARAMETERS
C
      WRITE(6,10) PNOT, W, F
10  FORMAT(025X, 'BEAM CHARACTERISTICS', //,
110X, 'PNOT = ', E12.3, 2X, 'WATTS', //,
210X, 'W = ', E12.3, 2X, 'METERS', //,
310X, 'F = ', E12.3, 2X, 'HERTZ', //)
      WRITE(6,12) KAPPA, ALPHA, THCON
12  FORMAT(025X, 'MATERIAL CHARACTERISTICS', //,
110X, 'KAPPA = ', 2X, E12.3, //,
210X, 'ALPHA = ', 2X, E12.3, //,
310X, 'THCON = ', 2X, E12.3, //)

C
C SET GRID SIZES - DEPENDENT UPON THE RELATIVE SIZE OF THE
C THERMAL WAVELENGTH WITH RESPECT TO THE SPOT SIZE AND ATTENUATION
C LENGTH
C
      TEMP(1)=CMPLX(0.,0.)
      TEMP(2)=CMPLX(0.,0.)
      DO 1111 M=1,2
      IF(M.EQ.2) F=1.E-9
      RR=FLOAT(RES)
      C1=DSQRT(KAPPA/(3.1416*F))/RR
      C2=W/RR
      IF(C1.LE.C2) GO TO 55
      GRIDAB(1) = C2
      GO TO 56
55  GRIDAB(1) = C1
56  C3=1./(ALPHA*RR)
      IF(C3.GT.C1) GO TO 57
      GRIDC(1)=C3

```

```

      GO TO 58
57  GRIDC(1)=C1
58  GRIDAB(2)=W/RR
      GRIDC(2)=1./(ALPHA*RR)
C
C      OUTPUT GRID DEFINITIONS
C
      WRITE (6,11) GRIDAB(M),GRIDC(M),NAB,NC,RES
11  FORMAT(025X,'INTEGRATION VALUES',//,
110X,'GRIDAB =',E12.3,2X,'METERS',/,
210X,'GRIDC =',E12.3,2X,'METERS',/,
310X,'NAB = ',I10,/,
410X,'NC = ',I10,/,
510X,'RESOLUTION = ',I10,/)
C
C      CALCULATE OTHER VARIABLES
C
      INOT=PNOT*2.0/(W**2*3.1416)
      KTHERM=DSQRT(3.1416*F/KAPPA)*(1.,1.)
      LTHERM = DSQRT(KAPPA/(3.1416*F))
C
C      OUTPUT OTHER VARIABLES
C
      WRITE(6,14) INOT,LTHERM
14  FORMAT(25X,'CALCULATED VALUES',//,
110X,'INOT =',2X,E12.3,/,
210X,'THERMAL WAVELENGTH - LTHERM =',2X,E12.3,/)
C
C      INTEGRATION
C
      ABMAX=(NAB*RR)+1
      CMAX=(NC*RR)+1
      DO 1010 CC=1,CMAX
      C=(FLOAT(CC)-.5)*GRIDC(M)
      DO 1000 AAB=1,ABMAX
      AB=(FLOAT(AAB)-.5)*GRIDAB(M)
      CALL TRAPS(2,2,2)
      PPV=ALPHA*INOT*EXP(-2*(AB**2)/W**2)*EXP(-ALPHA*C)
      R=SQRT(AB**2+C**2)
      TEMP(M)=TEMP(M)+(PPV/(R*THCON))*CDEXP(-KTHERM*R)*
      1AB*GRIDAB(M)*GRIDC(M)
1000 CONTINUE

```

```

1010 CONTINUE
C
C      OUTPUT RESULTS
C
      WRITE(6,1030) ABMAX,CMAX
1030 FORMAT(10X,'NUMBER OF SUMMATIONS',/,/,
110X,'ABMAX =',2X,I5,/,
310X,'CMAX =',2X,I5,/)
      WRITE(6,1080) TEMP(M)
1080 FORMAT(10X,'TEMPERATURE    REAL = ',2X,E12.5,/,
125X,'IMAG = ',2X,E12.5,/)
1111 CONTINUE
      TEMPM1 = TEMP(1) * DCONJG(TEMP(1))
      TEMPM1 = SQRT(TEMPM1)
      TEMPM2 = TEMP(2)*DCONJG(TEMP(2))
      TEMPM2 = SQRT(TEMPM2)
      WRITE(6,1040) TEMPM1
1040 FORMAT(10X,'AC TEMP MAGNITUDE FLUCTUATION = ',2X,E12.5,/)
      WRITE(6,1041) TEMPM2
1041 FORMAT(10X,'DC TEMP MAGNITUDE FLUCTUATION = ',2X,E12.5,/)
      RATIO = TEMPM2/TEMPM1
      WRITE(6,1042) RATIO
1042 FORMAT(10X,'RATIO  = ',2X,E12.5,/)
      STOP
      END
C
C INPUT DATA FORMAT
C
C PHOT,W,F,ALPHA
C THCON,RHO,CAP
C NAB,NC,RES
$DATA
1.E-3,.3E-6,1.E9,2.44E6
170.,2320.,712.
3,3,20

```

END

FILMED

4-85

DTIC